



# Pairwise Force Smoothed Particle Hydrodynamics model for multiphase flow: Surface tension and contact line dynamics



Alexandre M. Tartakovsky <sup>a,\*</sup>, Alexander Panchenko <sup>b</sup>

<sup>a</sup> Pacific Northwest National Laboratory, Richland, WA, USA

<sup>b</sup> Washington State University, Pullman, WA, USA

## ARTICLE INFO

*Article history:*

Received 6 December 2014

Received in revised form 22 August 2015

Accepted 25 August 2015

Available online 31 August 2015

*Keywords:*

Smoothed particle hydrodynamics

Multiphase flow

Surface tension

Contact line dynamics

Three-phase flow

Pore-scale flow

## ABSTRACT

We present a novel formulation of the Pairwise Force Smoothed Particle Hydrodynamics (PF-SPH) model and use it to simulate two- and three-phase flows in bounded domains. In the PF-SPH model, the Navier–Stokes equations are discretized with the Smoothed Particle Hydrodynamics (SPH) method, and the Young–Laplace boundary condition at the fluid–fluid interface and the Young boundary condition at the fluid–fluid–solid interface are replaced with pairwise forces added into the Navier–Stokes equations. We derive a relationship between the parameters in the pairwise forces and the surface tension and static contact angle. Next, we demonstrate the model's accuracy under static and dynamic conditions. Finally, we use the Pf-SPH model to simulate three phase flow in a porous medium.

© 2015 Elsevier Inc. All rights reserved.

## 1. Introduction

The flow of two or more fluid phases in a bounded domain is a complex problem, commonly described by multiphase Navier–Stokes equations. These equations have two nonlinearities: one is the standard inertial term, and another is due to the Young–Laplace and/or Young boundary conditions at the fluid–fluid and/or fluid–fluid–solid interfaces, respectively. Grid-based Eulerian computational fluid dynamics methods have been used to directly solve the multiphase Navier–Stokes equations, but they require computationally expensive interface tracking techniques. The phase-field [17], level-set [10], and volume-of-fluid [14,24,34] methods have been proposed to simplify interface tracking by introducing an additional field variable defining the position of the interface. In these methods, explicit tracking of the fluid–fluid interface is avoided at the cost of solving an additional hyperbolic equation for the field variable.

In addition to the non-linearity caused by moving fluid–fluid interfaces, the standard Navier–Stokes description presents two specific challenges for modeling multiphase flow in bounded domains: 1) there is an unphysical discontinuity in the fluid velocity across the fluid–fluid–solid interface [9]; and 2) a model relating the contact angle to the velocity of the contact line should be prescribed. Under static conditions, the static contact angle  $\theta_0$  can be easily measured and prescribed as a parameter for a given fluid–fluid–solid system. Under dynamic conditions, the contact angle  $\theta$  may have a complex, hysteretic behavior and is difficult to measure.

Different approximate models (e.g., creeping flow and lubrication flow [15]) for dealing with velocity discontinuity and phenomenological models [27,7,6] for dynamic contact angles have been proposed. Numerical solution of the resulting

\* Corresponding author. Tel.: +1 509 372 6185.

E-mail address: [alexandre.tartakovsky@pnnl.gov](mailto:alexandre.tartakovsky@pnnl.gov) (A.M. Tartakovsky).

equations, especially in geometrically complicated domains, can be difficult to obtain. As a result, few Eulerian models, based on a direct solution of the Navier–Stokes equations, have been used to model multiphase flow in domains with geometrically complicated boundaries, such as porous media. A review of numerical methods for pore-scale multiphase flows can be found in Meakin and Tartakovsky [19].

Here, we present a novel formulation of the Pairwise Force Smoothed Particle Hydrodynamics Model (PF-SPH) for multiphase Navier–Stokes equations. Smoothed Particle Hydrodynamics (SPH) is a Lagrangian method for solving conservation equations, including mass, momentum, and energy conservation equations [20]. SPH approximations of spatial derivatives are two-step. Differential operators are approximated with integrals, and integrals are approximated with Riemann sums. SPH is an attractive alternative to the Eulerian methods for solving interfacial problems. In SPH, each fluid phase is discretized with its own set of particles (discretization points) that are advected according to the equation of motion. There are two main approaches in SPH to impose the Young–Laplace boundary condition (and the surface tension) at the fluid–fluid interface and the Young condition (contact angle) at the fluid–fluid–solid interface. The first approach is based on the Continuum Boundary Force (CBF) method [5,21,13,1]. The second approach is the PF-SPH method [28,31,32,29,33]. In both approaches, the boundary conditions are replaced with forces that have non-zero net contributions only on SPH particles near the corresponding boundaries. In the CBF approach, these forces are directly computed from the boundary conditions. The advantage of this approach is that the surface tension and contact angle can be prescribed directly. On the other hand, as other Eulerian methods, the CBF-SPH approach must deal with non-physical stress singularity, and it requires a phenomenological model for the dynamic contact angle. In the PF-SPH method, the forces responsible for the Young–Laplace and Young boundary conditions are assumed to be pairwise molecular-like forces. As in the Molecular Dynamics method, the behavior of the fluid–fluid and fluid–fluid–solid interfaces in the PF-SPH model results from a force balance. Therefore, the PF-SPH method avoids the nonphysical stress singularity and does not require any knowledge of the contact angle dynamics. The PF-SPH method was extensively used for modeling two-phase flows, including liquid–gas flow and flow of two liquids in porous media. Until now, the analytical relationship between the pairwise forces and the continuum hydrodynamic parameters, such as surface tension and the contact angle, has not been established. Previously, the main disadvantage of the original PF-SPH model had been the need to calibrate the parameters in the pairwise forces with respect to the desired surface tension and static contact angle. The first step in establishing the correlation between the parameters in the PF-SPH model and the surface tension and contact angle has been made in Bandara et al. [3], based on Maxwell's theory of capillarity [18]. A good agreement between the PF-SPH model with the parameters estimated based on the Maxwell theory and multiphase microfluidic laboratory experiments has been observed in Bandara et al. [3], but some important questions with regard to the applicability of the Maxwell theory to the SPH method have remained unanswered. In his work, Maxwell derived a relationship between molecular pairwise forces and the surface tension, based on a “static view of the matter” [25]. In the SPH method, pressure gradient and viscous forces are implicitly many-body forces, dependent on local particle density, and the contribution of these forces to the surface tension cannot be readily explained by the Maxwell theory. Too, being a continuum approximation of the discrete molecular system, the Maxwell theory does not contain estimates of the resulting errors, which is important in applying it to a numerical method such as SPH.

In this paper, we derive relationships between parameters in the pairwise forces, surface tension, and static contact angle using thermodynamics considerations. We start by relating SPH forces to the stress in the fluid using the Hardy formula [11] and expressing surface tension as an integral of the difference of the normal and tangent components of the stress taken along a line normal to the interface using Gibbs thermodynamics theory [25]. To obtain a closed-form relationship between SPH forces, pressure, and surface tension, we approximate Hardy stress, given as a Riemann sum over all SPH particles, with an integral. This approximation is similar to the SPH approximation of spatial derivatives. Therefore, the accuracy of the resulting relationship between the pairwise forces and the surface tension is similar to the accuracy of the SPH discretization of spatial derivatives. Next, we show the accuracy of the PF-SPH method under static and dynamic conditions. Finally, to demonstrate the method's capabilities and robustness, we use it to simulate pore-scale flows of three fluids in a porous medium. To the best of our knowledge, this is the first model able to simulate pore-scale flow of three or more fluids.

## 2. Governing equations

Flow of two or more fluids is traditionally described by the Navier–Stokes equations written for each fluid phase  $\alpha$  in the form of the continuity equation:

$$\frac{D\rho_\alpha}{Dt} = -\rho_\alpha (\nabla \cdot \mathbf{v}_\alpha), \quad (1)$$

and the momentum conservation equation:

$$\rho_\alpha \frac{D\mathbf{v}_\alpha}{Dt} = -\nabla P_\alpha + \nabla \cdot \boldsymbol{\tau}_\alpha + \rho_\alpha \mathbf{g}, \quad (2)$$

where  $\mathbf{v}_\alpha$  is the velocity vector,  $\boldsymbol{\tau}_\alpha = [\mu_\alpha(\nabla \mathbf{v}_\alpha + \nabla \mathbf{v}_\alpha^T)]$  is the viscous stress tensor,  $\rho_\alpha$  is the density,  $P_\alpha$  is the pressure,  $\mu_\alpha$  is the dynamic viscosity,  $\mathbf{g}$  is the gravitational acceleration, and  $D/Dt = \partial/\partial t + \mathbf{v}_\alpha \cdot \nabla$  denotes a total derivative.

For generality, we treat the fluids as compressible and prescribe an equation of state (EOS)  $P_\alpha = f(\rho_\alpha)$  for each phase to close Eqs. (1) and (2). It is common to assume the no-slip boundary conditions for the fluid velocity at the fluid–solid boundary

$$v_{\alpha,n} = 0 \quad \text{and} \quad v_{\alpha,\tau} = 0; \quad (3)$$

the dynamic Young–Laplace boundary condition for pressure and velocity at the fluid–fluid interface

$$(P_\alpha - P_\beta)\mathbf{n} = (\boldsymbol{\tau}_\alpha - \boldsymbol{\tau}_\beta) \cdot \mathbf{n} + \kappa \sigma_{\alpha\beta} \mathbf{n}; \quad (4)$$

and to prescribe the contact angle  $\theta$  at the contact line (fluid–fluid–solid interface). Here,  $v_{\alpha,n}$  and  $v_{\alpha,\tau}$  are the normal and tangent components of velocity;  $\alpha$  and  $\beta$  denote the non-wetting and wetting phases, respectively;  $\kappa$  is the curvature of the interface; and  $\sigma_{\alpha\beta}$  is the surface tension between  $\alpha$  and  $\beta$  fluids. The normal vector  $\mathbf{n}$  is pointed away from the non-wetting phase. At equilibrium the (static) contact angle,  $\theta_0$ , is given by the Young formula

$$\sigma_{\alpha\beta} \cos \theta_0 + \sigma_{s\alpha} = \sigma_{s\beta}, \quad (5)$$

where  $\sigma_{s\alpha}$  and  $\sigma_{s\beta}$  are the superficial surface tension between the solid and fluid phases  $\alpha$  and  $\beta$ , respectively. Under dynamic conditions, the fluid–fluid–solid contact line moves, and the dynamic contact angle depends on the direction of flow and the magnitude of the velocity of the contact line. The advancing contact angle,  $\theta_a$ , formed by advancing wetting fluid, is greater than  $\theta_0$ , and the receding contact angle,  $\theta_r$ , formed by receding wetting fluid, is smaller than  $\theta_0$ . A number of phenomenological models exist for dynamic contact angles, including the exponential model [19]:

$$\theta_a - \theta_0 = a_a u^{b_a}, \quad \theta_0 - \theta_r = a_r u^{b_r}. \quad (6)$$

It should be noted that the combination of the no-slip boundary condition away from the contact line and the assumption that the contact line moves with non-zero velocity leads to a non-physical divergence of the viscous stress [9]. A review of grid-based Eulerian methods for modeling the contact line dynamics can be found in Bonn et al. [4].

### 3. PF-SPH multiphase flow model

In the multiphase PF-SPH model [32], various fluid and solid phases are represented by separate sets of particles. These particles serve as discretization points for the Navier–Stokes equations. The SPH method is based on a meshless interpolation scheme that allows estimation of a vector or scalar function  $A(\mathbf{r})$  (e.g., velocity, pressure, or density) at position  $\mathbf{r}$  in terms of the values of the function at the discretization points with positions  $\mathbf{r}_j$ :

$$A(\mathbf{r}) \approx \int A(\mathbf{r}') W(|\mathbf{r} - \mathbf{r}'|, h) d\mathbf{r}' \approx \sum_{j=1}^N \frac{A_j}{n_j} W(|\mathbf{r} - \mathbf{r}_j|, h), \quad (7)$$

where  $A_j = A(\mathbf{r}_j)$ ,  $N$  is the total number of SPH particles,  $n_j = \rho_j/m_j$  is the number density associated with point  $j$ ,  $m_j$  is the mass of particle  $j$ , and  $\rho_j = \rho(\mathbf{r}_j)$  is the fluid density. The function  $W$  is the SPH smoothing kernel with compact support  $h$  ( $W(|\mathbf{r}| > h) = 0$ ). Due to the compactness of  $W$ , the summation in Eq. (7) can be replaced with summation over just the particles within the distance  $h$  from  $\mathbf{r}$ . The smoothing kernel  $W$  must have at least a continuous first derivative and satisfy the normalization condition  $\int W(\mathbf{r} - \mathbf{r}', h) d\mathbf{r}' = 1$ , where integration is performed over the entire domain of  $A$ . In the limit  $h \rightarrow 0$ ,  $W$  is required to reduce to the Dirac delta function:  $\lim_{h \rightarrow 0} W(\mathbf{r} - \mathbf{r}', h) = \delta(\mathbf{r} - \mathbf{r}')$ . In this work, we use the fourth-order weighting function, which in two spatial dimensions has the form [22]:

$$W(|\mathbf{r}|, h) = \frac{189}{478\pi h^2} \tilde{W}^{(4)}(|\mathbf{r}|, h), \quad (8)$$

where

$$\tilde{W}^{(4)}(|\mathbf{r}|, h) = \begin{cases} \left(3 - \frac{3|\mathbf{r}|}{h}\right)^5 - 6\left(2 - \frac{3|\mathbf{r}|}{h}\right)^5 + 15\left(1 - \frac{3|\mathbf{r}|}{h}\right)^5 & 0 \leq |\mathbf{r}| < \frac{1}{3}h \\ \left(3 - \frac{3|\mathbf{r}|}{h}\right)^5 - 6\left(2 - \frac{3|\mathbf{r}|}{h}\right)^5 & \frac{1}{3}h \leq |\mathbf{r}| < \frac{2}{3}h \\ \left(3 - \frac{3|\mathbf{r}|}{h}\right)^5 & \frac{2}{3}h \leq |\mathbf{r}| < h \\ 0 & |\mathbf{r}| > h. \end{cases} \quad (9)$$

The number density  $n_j$  (the number of SPH particles within volume  $h^d$  centered at  $\mathbf{r}_j$ ) and  $h$  define the resolution of the SPH discretization scheme. For a sufficiently smooth  $A$ , the integral approximation (7) is second-order accurate in  $h$ . Approximating the integral in Eq. (7) with the sum introduces an additional error in the SPH discretization scheme that scales as  $n^{-1/d}$  [23].

The SPH discretization scheme (7) can be used to discretize the continuity equation (1). Alternatively, density  $m_i n_i$  can be found directly from Eq. (7) by replacing  $A_j$  with  $n_j$ :

$$n_i = \sum_{j=1}^N W(|\mathbf{r} - \mathbf{r}_j|, h). \quad (10)$$

The PF-SPH discretization of the momentum conservation equation (2), subject to the boundary condition (4), is given as:

$$\frac{D(m_i \mathbf{v}_i)}{Dt} = \mathbf{F}_i^P + \mathbf{F}_i^\mu + \mathbf{F}_i^{int} + \mathbf{F}^b. \quad (11)$$

Here,  $\mathbf{F}^b$  is the body force, and  $\mathbf{F}_i^P$  and  $\mathbf{F}_i^\mu$  are the “pressure gradient” and “viscous” forces given by an SPH discretization of the corresponding terms in the momentum conservation equation. In Eq. (11), the subscript  $\alpha$  is omitted for convenience. In multiphase fluid flows, wetting and non-wetting behaviors at the fluid–fluid–solid interface and pressure jump across the fluid–fluid boundary are a physical consequence of interactions between molecules of different fluid and solid phases. In the PF-SPH model, these physical phenomena are modeled by the molecular-like pairwise interaction forces,

$$\mathbf{F}_i^{int} = \sum_{j=1}^N \mathbf{F}_{ij}^{int} \quad \text{and} \quad \mathbf{F}_{ij}^{int} = -F_{\alpha\beta}^{int}(r_{ij}) \frac{\mathbf{r}_{ij}}{r_{ij}}, \quad (12)$$

acting between particle  $i$  of the  $\alpha$  phase and particle  $j$  of the  $\beta$  phase, where  $\beta$  can be a fluid or solid phase. In the above equations,  $\mathbf{r}_{ij} = \mathbf{r}_i - \mathbf{r}_j$  and  $r_{ij} = |\mathbf{r}_{ij}|$ . Like the pairwise molecular forces, the interaction forces  $\mathbf{F}_{ij}^{int}$  should be short-range repulsive ( $F_{\alpha\beta}^{int}(r_{ij} \leq r^*) < 0$ ,  $r^* < h$ ) and long-range attractive ( $F_{\alpha\beta}^{int}(r^* < r_{ij} \leq h) > 0$ ). For computational efficiency, the interaction force between two particles should be zero (or decay rapidly) for  $r_{ij} \geq h$ . The SPH equations are closed with an EOS:

$$P_\alpha = f_\alpha(n_\alpha). \quad (13)$$

The SPH discretization scheme (7) can be used to obtain  $\mathbf{F}_i^P$  and  $\mathbf{F}_i^\mu$  in different forms [20]. Because our focus is on the surface tension, which is not affected by the viscous force, here we consider only one form of  $\mathbf{F}_i^\mu$ , which is commonly used to model incompressible and weakly compressible fluids [22]:

$$\mathbf{F}_i^\mu = \sum_{j=1}^N \mathbf{F}_{ij}^\mu, \quad \mathbf{F}_{ij}^\mu = \frac{4\mu_i \mu_j}{\mu_i + \mu_j} \frac{\mathbf{v}_{ij}}{n_i n_j r_{ij}} \frac{dW(r_{ij}, h)}{dr_{ij}}, \quad (14)$$

where  $\mathbf{v}_{ij} = \mathbf{v}_i - \mathbf{v}_j$ .

Two common forms of

$$\mathbf{F}_i^P = \sum_{j=1}^N \mathbf{F}_{ij}^P \quad (15)$$

are

$$\mathbf{F}_{ij}^P = -\left(\frac{P_j}{n_j^2} + \frac{P_i}{n_i^2}\right) \frac{\mathbf{r}_{ij}}{r_{ij}} \frac{dW(r_{ij}, h)}{dr_{ij}} \quad (16)$$

and

$$\mathbf{F}_{ij}^P = -\frac{P_i + P_j}{n_i n_j} \frac{\mathbf{r}_{ij}}{r_{ij}} \frac{dW(r_{ij}, h)}{dr_{ij}}. \quad (17)$$

It is evident that for incompressible flows ( $n_i = n_j = \text{const}$ ) or (weakly) compressible flows with the ideal gas EOS  $P_i = cn_i$ , these two expressions are equivalent. On the other hand, for compressible fluids with non-linear EOS, these two expressions may produce different results. In Section 5.2 we show that Eq. (16) produces an artificial surface tension. Therefore, in any SPH multiphase model (including the PF-SPH model), it is preferable to discretize the pressure gradient term using Eq. (17).

The PF-SPH model (11) was originally proposed in Tartakovsky and Meakin [32] with  $F_{\alpha\beta}^{int}$  in the form:

$$F_{1,\alpha\beta}^{int}(r_{ij}) = \begin{cases} -s_{\alpha\beta} \cos\left(\frac{3\pi}{2h} r_{ij}\right) & r_{ij} \leq h \\ 0 & r_{ij} > h, \end{cases} \quad (18)$$

where  $s_{\alpha\beta}$  is the strength of the interaction force between particles of phases  $\alpha$  and  $\beta$ . The conservation of linear momentum requires  $s_{\alpha\beta} = s_{\beta\alpha}$ . Under this condition, the PF-SPH momentum equation (11) conserves linear momentum exactly. The immiscible behavior of the non-wetting and wetting phases is achieved by setting  $s_{\alpha\alpha} > s_{\alpha\beta}$  and  $s_{\beta\beta} > s_{\alpha\beta}$ . The wetting behavior of fluids is determined by the relative values of  $s_{\alpha\alpha}$ ,  $s_{\beta\beta}$ ,  $s_{\alpha\beta}$ ,  $s_{\beta\alpha}$ , and  $s_{\text{so}}$ . Here,  $s_{\alpha\alpha}$  and  $s_{\beta\beta}$  are the strength

of the pairwise forces acting between particles of the  $\alpha$  fluid and solid and the  $\beta$  fluid and solid, respectively. For the  $\beta$  fluid to wet the surface in the presence of the  $\alpha$  fluid (for the static contact angle to be less than 90 degrees), the following condition should be satisfied:

$$s_{\beta\beta}/s_{\beta\beta} > 1, \quad s_{\alpha\alpha}/s_{\alpha\alpha} < 1. \quad (19)$$

In Kordilla et al. [16],  $F_{\alpha\beta}$  was represented as a combination of two SPH weighting functions:

$$F_{4,\alpha\beta}^{int}(r_{ij}) = s_{\alpha\beta} \left[ -A \tilde{W}(r_{ij}, h^*) + \tilde{W}(r_{ij}, h) \right], \quad (20)$$

where  $A$  defines the ratio of magnitudes of the repulsive and attractive parts of the force  $\mathbf{F}_{ij}^{int}$  and  $h^*$  and  $h$  ( $h^* < h$ ) determine ranges of the repulsive and attractive parts of the force, respectively. In this paper, we consider four different forms of  $F_{\alpha\beta}^{int}$ , which are listed in Table 1. In Section 5.3, we demonstrate that the form of  $\mathbf{F}_{ij}^{int}$  and the choice of parameters affect the distribution of SPH particles. The particle distribution is an important consideration in any variant of the SPH method as it affects the accuracy of the SPH discretization.

There are several approaches in SPH to impose the no-slip boundary condition at the fluid–solid boundary away from the fluid–fluid–solid interface. In this work, we approximately impose the no-slip boundary condition by assigning zero velocity to the solid particles and including the solid particles in evaluation of the  $\mathbf{F}_i^P$ ,  $\mathbf{F}_i^\mu$ , and  $\mathbf{F}_i^{int}$  forces acting on the fluid particles. The particle density of the solid particles is evaluated in the same way as the density of fluid particles (i.e., from Eq. (10)). When computing  $\mathbf{F}_i^P$ , the EOS of solid particle  $j$  is assumed to be the same as the EOS of fluid particle  $i$ . In the expression for  $\mathbf{F}_i^\mu$ , the viscosity of solid particle  $j$  is assumed to be the same as the viscosity of fluid particle  $i$ . For single-phase flows, more accurate implementations of the no-slip boundary condition have been proposed [22,12]. Extending these methods for the multiphase PF-SPH method is a subject of our future research.

We integrate the SPH equations using the “velocity Verlet” algorithm [2,28,31,16]:

$$\mathbf{r}_i(t + \Delta t) = \mathbf{r}_i(t) + \Delta t \mathbf{v}_i(t) + \frac{\Delta t^2}{2m_i} \mathbf{f}_i(t) \quad (21)$$

$$\mathbf{v}_i(t + \Delta t) = \mathbf{v}_i(t) + \frac{\Delta t}{2m_i} [\mathbf{f}_i(t) + \mathbf{f}_i(t + \Delta t)]. \quad (22)$$

Here,  $\mathbf{f}_i(t + \Delta t) = \mathbf{F}_i^P(t + \Delta t) + \mathbf{F}_i^\mu(t + \Delta t) + \mathbf{F}_i^{int}(t + \Delta t) + \mathbf{g}$ ,  $\mathbf{F}_i^P(t + \Delta t)$  and  $\mathbf{F}_i^{int}(t + \Delta t)$  are computed using particle positions at time  $(t + \Delta t)$ ,  $\mathbf{F}_i^\mu(t + \Delta t)$  is found using particle positions at time  $(t + \Delta t)$  and velocities at time  $t$ , and the time step  $\Delta t$  satisfies the constraints [22]:

$$\begin{aligned} \Delta t &\leq 0.25 \min_i \left( \frac{h}{3|\mathbf{v}_i|} \right), \\ \Delta t &\leq 0.25 \min_i \left( \sqrt{\frac{m_i h}{3|\mathbf{f}_i|}} \right), \\ \Delta t &\leq 0.25 \min_i \left( \frac{\rho_i h^2}{9\mu} \right). \end{aligned} \quad (23)$$

In the past, the PF-SPH multiphase model has been validated under both static and dynamic conditions for different forms of  $\mathbf{F}_{ij}^{int}$  [32,16]. The first step in these validation studies was to determine the surface tension and the static contact angle for a prescribed set of parameters in  $\mathbf{F}_{ij}^{int}$ . The surface tension was determined from the Young–Laplace equation by simulating a bubble of one fluid surrounded by another fluid. The static contact angle was measured by simulating a bubble resting on a horizontal surface. In the second step of the validation studies, the two-phase flow was simulated under dynamic conditions, and the results were compared with the corresponding analytical solutions and/or experimental results. It was also shown that the PF-SPH model can model multiphase flows with density ratios as large as 1000 and viscosity ratios as large as 100 [33]. Until now, the primary disadvantage of the PF-SPH multiphase model was the need to calibrate the parameters in  $\mathbf{F}_{ij}^{int}$  with respect to surface tension and static contact angle.

In Section 4, we demonstrate that the parameters, in  $\mathbf{F}_{ij}^{int}$  can be related to macroscopic parameters, such as  $\sigma_{\alpha\beta}$  and  $\theta_0$ , via closed-form analytical expressions. Therefore, the validation cases presented in this paper mainly focus on testing these analytical expressions. We also demonstrate that the PF-SPH model is able to reproduce Tanner’s Law for a bubble spreading on the surface. In addition, we study flow of a droplet between two parallel plates to demonstrate that the resulting velocity and contact angles satisfy the corresponding analytical solution. Next, we show that the receding and advancing contact angles change as a power of the droplet velocity—behavior also observed in experiments. In the last section, we present simulations of three-phase flow in porous media. The latter numerical examples demonstrate robustness of the PF-SPH model, i.e., these simulations show that the PF-SPH model can simulate complex flows in domains with complicated geometry.

#### 4. Direct calculation of surface tension from the total stress

In SPH, as in any Lagrangian particle model, the total stress in the fluid at point  $\mathbf{x}$  can be found according to the Hardy formula [11]:

$$\mathbf{T}(\mathbf{x}) = \mathbf{T}_{(c)}(\mathbf{x}) + \mathbf{T}_{(int)}(\mathbf{x}), \quad (24)$$

where  $\mathbf{T}_{(c)}(\mathbf{x})$  is the convection stress,

$$\mathbf{T}_{(c)}(\mathbf{x}) = - \sum_{j=1}^N m_j (\bar{\mathbf{v}}(\mathbf{x}) - \mathbf{v}_j) \otimes (\bar{\mathbf{v}}(\mathbf{x}) - \mathbf{v}_j) \tilde{\psi}_\eta(\mathbf{x} - \mathbf{r}_j), \quad (25)$$

and  $\mathbf{T}_{(int)}(\mathbf{x})$  is the interaction stress,

$$\mathbf{T}_{(int)}(\mathbf{x}) = \frac{1}{2} \sum_{i=1}^N \sum_{j=1}^N \mathbf{f}_{ij} \otimes (\mathbf{r}_j - \mathbf{r}_i) \int_0^1 \tilde{\psi}_\eta(\mathbf{x} - s\mathbf{r}_i - (1-s)\mathbf{r}_j) ds, \quad (26)$$

where  $\bar{\mathbf{v}}(\mathbf{x}) = \sum_j m_j \mathbf{v}_j \tilde{\psi}_\eta(\mathbf{x} - \mathbf{r}_j) \left( \sum_j m_j \tilde{\psi}_\eta(\mathbf{x} - \mathbf{r}_j) \right)^{-1}$  is the average velocity and  $\mathbf{f}_{ij}$  is the total force acting on the particles. In the absence of gravity, in the PF-SPH model this force is given as:

$$\mathbf{f}_{ij} = \mathbf{F}_{ij}^P + \mathbf{F}_{ij}^\mu + \mathbf{F}_{ij}^{int}. \quad (27)$$

The summation here is over all particles, and  $\otimes$  denotes the dyadic product of vectors. The choice of the weighting function  $\tilde{\psi}(\mathbf{x})$  is fairly arbitrary, and here we assume that  $\tilde{\psi}(\mathbf{x})$  is the product of one-dimensional functions  $\psi_{\eta,l} = \frac{1}{\eta} \psi(\mathbf{x}_{(l)})$ , where  $l = 1, 2, 3$  denotes a component of the vector. The function  $\psi_{\eta,l}(\mathbf{x})$  has the compact support  $\eta$  or becomes sufficiently small for  $|\mathbf{r}| > \eta$ . The support  $\eta$  should be greater than  $h$  and smaller than the size of the domain. In our calculations, we set  $\eta = 2h$ . At the static equilibrium ( $\mathbf{v}_i = 0$  for  $i = 1, \dots, N$ ),  $\mathbf{T}_{(c)}(\mathbf{x}) = 0$ , and  $\mathbf{T}(\mathbf{x})$  reduces to  $\mathbf{T}(\mathbf{x}) = \mathbf{T}_{(int)}(\mathbf{x})$ . In a bulk fluid (away from the fluid–fluid interface),  $\mathbf{T}(\mathbf{x})$  becomes a diagonal tensor with the diagonal components  $T_{xx} = T_{yy} = T_{zz} = -p$ , where  $p$  is the “total” pressure. It should be noted that in the PF-SPH model,  $p$  is the sum of  $P$  and the virial pressure generated by the  $\mathbf{F}_{ij}^{int}$  forces.

Consider two fluid phases  $\alpha$  and  $\beta$  separated by a flat interface perpendicular to the  $z$  direction. From symmetry considerations, the off-diagonal components of  $\mathbf{T}$  are zero, the diagonal components depend only on  $z$ , and  $T_{xx}(z) = T_{yy}(z) = T_\tau(z)$ . Then, based on the Gibbs treatment of thermodynamics, the surface tension can be found as [25]:

$$\sigma_{\alpha\beta} = \int_{-\infty}^{+\infty} [T_\tau(z) - T_n(z)] dz, \quad (28)$$

where  $T_n(z) = T_{zz}(z)$  and  $T_\tau(z)$  are the normal and tangent components of the stress. In a two-dimensional space for two fluids separated by a flat interface parallel to the  $x$  direction, similar arguments yield Eq. (28) with

$$T_n(y) = T_{yy} \quad \text{and} \quad T_\tau(y) = T_{xx}(y). \quad (29)$$

[Fig. 1](#) shows components of the stress tensor obtained from an SPH simulation of two fluids separated by a flat front located at  $y = 16h$  after the fluid system reached equilibrium. In this simulation, at time zero, the SPH particles are randomly placed in a domain  $16h \times 32h$  with the average particle density  $n_{eq} = 36$ , which is achieved by dividing the domain into  $1h$  by  $1h$  square subdomains and randomly placing 36 particles in each. The SPH particles in the lower half of the domain (with the  $y$ -coordinate less than  $16h$ ) are labeled as  $\alpha$  particles, and the remaining particles are labeled as  $\beta$  particles. Then, the positions of particles are evolved according to the SPH momentum conservation equation. [Fig. 1\(a\)](#) displays the components of  $\mathbf{T}(x = 8, y)$ , and [Fig. 1\(b\)](#) shows the components of  $\mathbf{T}(x, y)$  averaged over the  $x$  direction,  $\bar{\mathbf{T}}(y) = \frac{1}{N} \sum_{i=1}^N \mathbf{T}(x_i, y)$ . The stress is computed using the two-dimensional version of Eq. (26) after the system reaches equilibrium. Due to particle disorder, both components of  $\mathbf{T}(\mathbf{x})$  vary with  $y$ , and, as follows from the equilibrium condition  $\nabla \cdot \mathbf{T} = 0, x$ , which violates the condition (29). This means that on the particle level, the interface is not flat. On the other hand, the components of the average stress  $\bar{\mathbf{T}}(\mathbf{x})$  satisfy the condition for stress at a flat interface, i.e.,  $\bar{T}_{yy}$  is constant and  $\bar{T}_{xx}$  depends only on  $y$ . Then, the surface tension is equal to the area between the two curves in [Fig. 1\(b\)](#).

Next, we simulate a two-dimensional bubble of the fluid  $\alpha$  surrounded by the fluid  $\beta$  using the same parameters as in the simulation with a flat front (as already described). The bubble is located in the center of a  $32h \times 32h$  domain and has radius  $8h$ . [Fig. 2](#) shows the stress components  $T_{xx}(x = 16, y) = T_\tau(x = 16, y)$  and  $T_{yy}(x = 16, y) = T_n(x = 16, y)$  as a function of  $y$  after the system reaches equilibrium. The  $T_{yy}$ -component at point  $(x = 16, y = 24)$  is normal to the interface and, therefore, is equal to the negative total pressure  $-p$ . It can be seen that  $p$  changes gradually across the interface from the larger value inside the bubble to the smaller value outside of the bubble. The transition zone is on the order of  $2\eta$ . As before, the surface tension is given by the area between the  $T_{xx}$  and  $T_{yy}$  curves.

In [Appendix A](#) we perform an analytical integration in Eq. (28) to obtain closed-form relationships between the surface tension and parameters in the SPH forces.

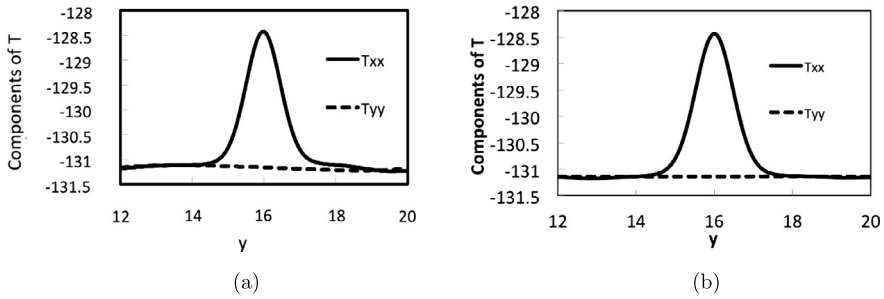


**Fig. 1.**  $T_{xx}$  and  $T_{yy}$  components of stress as a function of  $y$  obtained from a simulation of two fluids separated by flat interface located at  $y = 16$ . In the simulation, the pairwise force  $F_{2,\alpha\beta}^{int}(r_{ij}) = s_{\alpha\beta} [-A\psi_{\varepsilon_0}(r_{ij}) + \psi_\varepsilon(r_{ij})]$  is used with  $s_{ww} = s_{nn} = 2$ ,  $n_w = n_n = 36$ ,  $s_{nw} = 0.00001$ ,  $\varepsilon = h/3.5$ ,  $\varepsilon_0 = \varepsilon/2$ , and  $A = \varepsilon^2/\varepsilon_0^2$ .

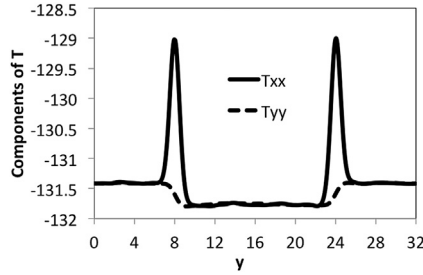


**Fig. 2.** Tangent ( $T_{xx}$ ) and normal ( $T_{yy}$ ) components of stress as a function of the radial coordinate ( $y - 8$ ) obtained from a simulation of a droplet of fluid  $\alpha$  separated by fluid  $\beta$ . The center of the two-dimensional droplet is at  $x = y = 16$ , and the radius is equal to 8. In the simulation, the pairwise force  $F_{2,\alpha\beta}^{int}(r_{ij}) = s_{\alpha\beta} \left[ -A\psi_{\varepsilon_0}(r_{ij}) + \psi_\varepsilon(r_{ij}) \right]$  is used with  $s_{ww} = s_{nn} = 2$ ,  $n_w = n_n = 36$ ,  $s_{nw} = 0.00001$ ,  $\varepsilon = h/3.5$ ,  $\varepsilon_0 = \varepsilon/2$ , and  $A = \varepsilon^2/\varepsilon_0^2$ .

## 5. Relationship between the pairwise forces and macroscopic parameters

### 5.1. Virial pressure due to pairwise forces

Under static conditions, the force  $\mathbf{f}_{ij}$ , acting between particle  $i$  of phase  $\alpha$  and particle  $j$  of phase  $\beta$ , can be written as:

$$\mathbf{f}_{ij} = \phi_{\alpha\beta}(r_{ij}) \frac{\mathbf{r}_{ij}}{r_{ij}} = -[F_{\alpha\beta}^p(r_{ij}) + F_{\alpha\beta}^{int}(r_{ij})] \frac{\mathbf{r}_{ij}}{r_{ij}}, \quad (30)$$

where  $\phi_{\alpha\beta}(r_{ij}) = -[F_{\alpha\beta}^P(r_{ij}) + F_{\alpha\beta}^{int}(r_{ij})]$  and  $\phi_{\alpha\beta}^P$  is given, depending on the choice of discretization, by

$$F_{\alpha\beta}^P(z) = \left( \frac{P_\alpha}{n_\alpha^2} + \frac{P_\beta}{n_\beta^2} \right) \frac{dW(z)}{dz} \quad (31)$$

or

$$F_{\alpha\beta}^P(z) = \frac{P_\alpha + P_\beta}{n_\alpha n_\beta} \frac{dW(z)}{dz}. \quad (32)$$

In Appendix B, we demonstrate that away from the interface (at the normal distance from the interface greater than  $\eta$ ), the stress component  $\mathbf{T}_{(int)}$  is a diagonal tensor  $\mathbf{T}_{(int)} = -p\mathbf{I}$ , where  $p$  is the total pressure that can be found analytically by approximating the double sum in Eq. (26) with the double integral as:

$$p_\alpha = -\frac{2}{3}\pi n_\alpha n_\alpha \int_0^\infty z^3 [F_{\alpha\alpha}^P(z) + F_{\alpha\alpha}^{int}(z)] dz \quad (33)$$

in three spatial dimensions and

$$p_\alpha = -\frac{1}{2}\pi n_\alpha n_\alpha \int_0^\infty z^2 [F_{\alpha\alpha}^P(z) + F_{\alpha\alpha}^{int}(z)] dz \quad (34)$$

in two dimensions. Here, the subscript  $\alpha$  emphasizes that  $p_\alpha$  is the pressure in the  $\alpha$  phase. It can be easily verified that

**Table 1**

Virial pressure,  $p_\alpha = -\xi n_\alpha^2 s_{\alpha\alpha}$ , and specific energy,  $T_{\alpha\beta} = \lambda n_\alpha n_\beta s_{\alpha\beta}$ , due to different pairwise forces  $\mathbf{F}_{ij}^{int} = -F_{k,\alpha\beta}^{int}(r_{ij}) \frac{\mathbf{r}_{ij}}{r_{ij}}$  ( $k = 1, 2, 3, 4$ ) in two and three spatial dimensions. In  $F_{2,\alpha\beta}^{int}$  and  $F_{3,\alpha\beta}^{int}$ ,  $\psi_\epsilon(r_{ij}) = e^{-\frac{r_{ij}^2}{2\epsilon^2}}$ ,  $\epsilon = h/3.5$ , and  $\psi_{\epsilon_0}(r_{ij}) = e^{-\frac{r_{ij}^2}{2\epsilon_0^2}}$ .

$F_{1,\alpha\beta}^{int}(r_{ij}) = -s_{\alpha\beta} \cos\left(\frac{3\pi}{2h} r_{ij}\right)$ if $0 \leq r_{ij} \leq h$ ; $F_{1,\alpha\beta}^{int}(r_{ij}) = 0$ if $r_{ij} > h$
3D: $\xi = \frac{16}{81} \frac{h^4}{\pi^3} \left[ \frac{9}{4}\pi^3 - 6\pi - 4 \right]$
2D: $\xi = \frac{h^3(-8+9\pi^2)}{27\pi^2}$
3D: $\lambda = \frac{3}{4\pi^4} [2^7 - 3^2 \times 2^4\pi^2 + 3^3\pi^4] \left(\frac{h}{3}\right)^5$
2D: $\lambda = \frac{8}{81} \frac{h^4}{\pi^4} \left[ \frac{9}{4}\pi^3 - 6\pi - 4 \right]$
$F_{2,\alpha\beta}^{int}(r_{ij}) = s_{\alpha\beta} [-A\psi_{\epsilon_0}(r_{ij}) + \psi_\epsilon(r_{ij})]$ , $\epsilon/\epsilon_0 = 2$
3D: $A = (\epsilon/\epsilon_0)^3$ , and 2D: $A = (\epsilon/\epsilon_0)^2$
3D: $\xi = \frac{4\pi}{3} [-A\epsilon_0^4 + \epsilon^4]$
2D: $\xi = \frac{\pi\sqrt{\pi}}{2\sqrt{2}} [-A\epsilon_0^3 + \epsilon^3]$
3D: $\lambda = (2\pi)^{3/2} \frac{3}{32} (-A\epsilon_0^5 + \epsilon^5)$
2D: $\lambda = \frac{2}{3} (-A\epsilon_0^4 + \epsilon^4)$ .
$F_{3,\alpha\beta}^{int}(r_{ij}) = s_{\alpha\beta} r_{ij} [-A\psi_{\epsilon_0}(r_{ij}) + \psi_\epsilon(r_{ij})]$ , $\epsilon/\epsilon_0 = 2$
3D: $A = (\epsilon/\epsilon_0)^4$ , and 2D: $A = (\epsilon/\epsilon_0)^3$
3D: $\xi = \sqrt{2}\pi^{3/2} [-A\epsilon_0^5 + \epsilon^5]$
2D: $\xi = \pi [-A\epsilon_0^4 + \epsilon^4]$
3D: $\lambda = \pi (-A\epsilon_0^6 + \epsilon^6)$
2D: $\lambda = \frac{1}{2} \sqrt{2\pi} (-A\epsilon_0^5 + \epsilon^5)$
$F_{4,\alpha\beta}^{int}(r_{ij}) = s_{\alpha\beta} \left[ -A\tilde{W}_{h_0}^{(4)}(r_{ij}) + \tilde{W}_h^{(4)}(r_{ij}) \right]$ , $h/h_0 = 2$
3D: $A = (h/h_0)^3$ , and 2D: $A = (h/h_0)^2$
3D: $\xi = \frac{2771}{10206} \pi [-Ah_0^4 + h^4]$
2D: $\xi = \frac{5}{9} \pi [-Ah_0^3 + h^3]$
3D: $\lambda = \frac{7}{324} \pi (-Ah_0^5 + h^5)$
2D: $\lambda = \frac{2771}{20421} (-Ah_0^4 + h^4)$

$$-\frac{2}{3}\pi n_\alpha n_\alpha \int_0^\infty z^3 F_{\alpha\alpha}^P(z) dz = P_\alpha \quad (35)$$

in three spatial dimensions and

$$-\frac{1}{2}\pi n_\alpha n_\alpha \int_0^\infty z^2 F_{\alpha\alpha}^P(z) dz = P_\alpha \quad (36)$$

in two spatial dimensions. The last two expressions show that the pressure generated by the forces  $\mathbf{F}_i^P$  is exactly equal to the pressure prescribed by the EOS, confirming the consistency of Eqs. (33) and (34). In the following, we refer to the pressure generated by forces  $\mathbf{F}_{ij}^{int}$  as the “virial pressure.”

Table 1 gives functional expressions for the virial pressure generated by various forms of  $\mathbf{F}_{ij}^{int}$  in two and three spatial dimensions. The virial pressure generated by  $F_{1,\alpha\beta}^{int}$  is always negative, regardless of the choice of parameters. The virial pressure due to the pairwise forces with  $F_{k,ij}^{int}$ ,  $k = 2, 3, 4$  in Table 1 (which are given by a combination of two Gaussian or polynomial functions) can be positive or negative and may be eliminated by choosing a certain value of the parameter  $A$ . For example, in two spatial dimensions, the virial pressure generated by  $F_{2,ij}^{int}$  can be eliminated by setting  $A = \epsilon^4/\epsilon_0^4$ . At the same time, the parameter  $A$  affects distribution of the SPH particles, both in the bulk and near the fluid–fluid interface. Our simulations show that a negative virial pressure is needed to generate a stable interface between two fluids and a uniform particle distribution. Table 1 lists the values of the parameter  $A$  used in the presented here simulations.

## 5.2. Surface tension and contact angles

Approximating double summation in the definition of stress  $\mathbf{T}$  with double integral, substituting this in the expression (28) for  $\sigma_{\alpha\beta}$ , and integrating the latter analytically, we demonstrate that the surface tension between fluids  $\alpha$  and  $\beta$  can be found as (Appendix A):

$$\sigma_{\alpha\beta} = \mathcal{T}_{\alpha\alpha} + \mathcal{T}_{\beta\beta} - 2\mathcal{T}_{\alpha\beta}, \quad (37)$$

where  $\mathcal{T}_{\alpha\beta}$  is the specific interfacial energy between  $\alpha$  and  $\beta$  fluid phases and  $\mathcal{T}_{\alpha\alpha}$  and  $\mathcal{T}_{\beta\beta}$  are the specific energies in  $\alpha$  and  $\beta$  phases, respectively.

For three fluids in contact with each other, the surface tensions between each pair of fluids and contact angles, formed by the fluid–fluid boundaries, satisfy at the equilibrium the following conditions:

$$\sigma_{13}\cos\theta_1 + \sigma_{23}\cos\theta_2 + \sigma_{12} = 0$$

$$\sigma_{12}\cos\theta_1 + \sigma_{23}\cos\theta_3 + \sigma_{13} = 0$$

$$\sigma_{12}\cos\theta_2 + \sigma_{13}\cos\theta_3 + \sigma_{23} = 0.$$

Two fluids in contact with the solid surface form the contact angle, an angle between the solid surface and fluid–fluid interface bounding the  $\alpha$ -fluid. At the equilibrium, this angle is commonly referred to as the “static contact angle,”  $\theta_0$ , and is given by Young’s equation (5).

In Appendix A, we derive an expression for  $\mathcal{T}_{\alpha\beta}$  in terms of  $\phi_{\alpha\beta}$ . In three dimensions,  $\mathcal{T}_{\alpha\beta}$  is given by

$$\mathcal{T}_{\alpha\beta} = -\frac{1}{8}\pi n_\alpha n_\beta \int_0^\infty z^4 \phi_{\alpha\beta}(z) dz, \quad (\alpha, \beta) = n, w, s, \quad (38)$$

and in two dimensions by

$$\mathcal{T}_{\alpha\beta} = -\frac{1}{3}n_\alpha n_\beta \int_0^\infty z^3 \phi_{\alpha\beta}(z) dz, \quad (\alpha, \beta) = n, w, s. \quad (39)$$

In the derivation of  $\mathcal{T}_{\alpha\beta}$ , we assume that the radii of the front curvature are much larger than  $h$  (i.e., the front can be locally approximated as flat), and the thickness of each phase (the dimension in the direction normal to the interface) is larger than  $h$ , the range of interaction of the pairwise forces. For the radii of the front curvature larger than  $h$ , the surface tension should be independent on the front curvature. Therefore, Eq. (39) should hold for fronts with any well-resolved front curvature. It is also assumed that the number density within each phase is constant. For the three-dimensional space, our expression is identical to that of Maxwell [18], who considered fluids made of particles that interact with each other via pairwise forces. In Appendix A, we present derivations for only the two-dimensional problem.

In the following, we calculate  $\mathcal{T}_{\alpha\beta}$  under static conditions ( $\mathbf{v}_i = [0, 0, 0]^T$ ) as this allows us to derive an analytical closed-form expression for  $\mathcal{T}_{\alpha\beta}$  as a function of the parameters in  $\mathbf{F}_{ij}^{int}$ . Because the surface tension is the same under both dynamic and static conditions, the resulting relationship between the surface tension and parameters in the SPH model also is applicable under both conditions.

We can write  $\mathcal{T}_{\alpha\beta}$  as:

$$\mathcal{T}_{\alpha\beta} = \mathcal{T}_{\alpha\beta}^P + \mathcal{T}_{\alpha\beta}^{int}, \quad (\alpha, \beta) = n, w, s, \quad (40)$$

where  $\mathcal{T}_{\alpha\beta}^P$  is the component of energy because of the  $\mathbf{F}_{ij}^P$  forces and  $\mathcal{T}_{\alpha\beta}^{int}$  is the component of energy due to the  $\mathbf{F}_{ij}^{int}$  forces. Furthermore, we write the surface tension as

$$\sigma_{\alpha\beta} = \sigma_{\alpha\beta}^P + \sigma_{\alpha\beta}^{int}, \quad (41)$$

where  $\sigma_{\alpha\beta}^P$  and  $\sigma_{\alpha\beta}^{int}$  are the contributions to the surface tension from the pressure gradient and pairwise forces, respectively, and are given by

$$\sigma_{\alpha\beta}^P = \mathcal{T}_{\alpha\alpha}^P + \mathcal{T}_{\beta\beta}^P - 2\mathcal{T}_{\alpha\beta}^P \quad \text{and} \quad \sigma_{\alpha\beta}^{int} = \mathcal{T}_{\alpha\alpha}^{int} + \mathcal{T}_{\beta\beta}^{int} - 2\mathcal{T}_{\alpha\beta}^{int}. \quad (42)$$

Substituting Eqs. (31) and (32) into Eq. (38) in three dimensions and Eq. (39) in two dimensions yields the following expressions for the partial surface energy as a result of the pressure gradient force:

$$\mathcal{T}_{\alpha\beta}^P = \gamma n_\alpha n_\beta \left( \frac{P_\alpha}{n_\alpha^2} + \frac{P_\beta}{n_\beta^2} \right) \quad (43)$$

or

$$\mathcal{T}_{\alpha\beta}^P = \gamma(P_\alpha + P_\beta), \quad (44)$$

depending on the SPH discretization of the pressure gradient. Here,  $\gamma = \frac{1}{8}\pi \int_0^\infty z^4 \frac{dW}{dz} dz$  and  $\gamma = \frac{1}{3} \int_0^\infty z^3 \frac{dW}{dz} dz$  in three and two dimensions, respectively. Note that  $\gamma < 0$  in both two and three dimensions.

The partial surface energy due to the interaction force is given by

$$\mathcal{T}_{\alpha\beta}^{\text{int}} = \frac{1}{8}\pi n_{\alpha}n_{\beta} \int_0^{\infty} z^4 F_{\alpha\beta}^{\text{int}}(z) dz = \lambda n_{\alpha}n_{\beta} s_{\alpha\beta} \quad (45)$$

and

$$\mathcal{T}_{\alpha\beta}^{\text{int}} = \frac{1}{3}n_{\alpha}n_{\beta} \int_0^{\infty} z^3 F_{\alpha\beta}^{\text{int}}(z) dz = \lambda n_{\alpha}n_{\beta} s_{\alpha\beta} \quad (46)$$

in three and two spatial dimensions, respectively. The parameter  $\lambda$  depends on the range and specific form of  $F_{\alpha\beta}^{\text{int}}$  and the number of spatial dimensions. Knowing the “partial” surface energies, the “partial” surface tensions due to  $\mathbf{F}_{ij}^P$  and  $\mathbf{F}_{ij}^{\text{int}}$  can be determined. In the following, we consider the contribution of partial surface tensions,  $\sigma_{\alpha\beta}^P$  and  $\sigma_{\alpha\beta}^{\text{int}}$ , to the “total” surface tension,  $\sigma_{\alpha\beta}$ , starting with  $\sigma_{\alpha\beta}^P$ . First, we note that for incompressible fluids,  $\sigma_{\alpha\beta}^P$  based on Eq. (43) is

$$\sigma_{\alpha\beta}^P = -2\gamma(P_{\alpha} + P_{\beta} - \frac{n_{\beta}}{n_{\alpha}}P_{\alpha} - \frac{n_{\alpha}}{n_{\beta}}P_{\beta}), \quad (47)$$

and  $\sigma_{\alpha\beta}^P$  based on Eq. (44) is

$$\sigma_{\alpha\beta}^P = 0. \quad (48)$$

The pressure gradient term in the Navier-Stokes equations does not generate the surface tension (the surface tension should be prescribed, for example, via the Young-Laplace boundary condition), and the SPH discretization (17) explicitly enforces this condition. On the other hand, the SPH discretization (16) produces “numerical” surface tension if different resolution  $n$  is used to discretize different fluid phases. Therefore, in the multiphase SPH flow models, it is necessary to discretize the pressure gradient term according to Eq. (17). We should note that for compressible fluids with linear EOS such as the ideal gas EOS

$$P_i = k_b T n_i, \quad (49)$$

these two discretizations of the pressure gradient become identical. In this EOS,  $k_b$  is the Boltzmann constant and  $T$  is temperature.

The ideal gas EOS can be modified as:

$$P_i = c_{\alpha\beta} n_i. \quad (50)$$

Substituting the EOS (50) in Eq. (44) results in the force

$$c_{\alpha\beta} \frac{n_{\alpha}n_{\beta}}{n_{\alpha}n_{\beta}} \frac{dW}{dz} \frac{\mathbf{r}_{ij}}{r_{ij}} \quad (51)$$

between particle  $i$  of phase  $\alpha$  and particle  $j$  of phase  $\beta$  with the strength  $c_{\alpha\beta}$ , which can be different for interactions between particles of different phases. Because the EOS (50) produces purely repulsive forces, to generate surface tension between  $\alpha$  and  $\beta$  phases, one should set  $c_{\alpha\beta} > c_{\alpha\alpha}$  and  $c_{\alpha\beta} > c_{\beta\beta}$ , resulting in the surface tension:

$$\sigma_{\alpha\beta}^P = 2\gamma(n_{\alpha}c_{\alpha\alpha} + n_{\beta}c_{\beta\beta} - n_{\beta}c_{\alpha\beta} - n_{\alpha}c_{\beta\alpha}). \quad (52)$$

For incompressible and weakly compressible fluids, we can assume that  $n_{\alpha} = n_{\beta} = n_{eq}$ , resulting in

$$\sigma_{\alpha\beta}^P = 2\gamma n_{eq}(c_{\alpha\alpha} + c_{\beta\beta} - 2c_{\alpha\beta}). \quad (53)$$

Tartakovsky et al. [30] proposed to use the van der Waals (vdW) EOS

$$P = \frac{k_b T n}{1 - b n} - a_{\alpha\beta} n^2 \quad (54)$$

to generate surface tension in the PF-SPH model. Substituting the vdW EOS into Eq. (44) yields

$$\mathcal{T}_{\alpha\beta}^P = \gamma \left( \frac{k_b T n_{\alpha}}{1 - b n_{\alpha}} + \frac{k_b T n_{\beta}}{1 - b n_{\beta}} - a_{\alpha\beta} (n_{\alpha}^2 + n_{\beta}^2) \right) \quad (55)$$

and

$$\sigma_{\alpha\beta}^P = -2\gamma \left( a_{\alpha\alpha} n_{\alpha}^2 + a_{\beta\beta} n_{\beta}^2 - a_{\alpha\beta} (n_{\alpha}^2 + n_{\beta}^2) \right). \quad (56)$$

To generate surface tension with the vdW EOS (54), it is sufficient to have  $a_{\alpha\alpha} > a_{\alpha\beta}$  and  $a_{\beta\beta} > a_{\alpha\beta}$ . In the following, we will refer to EOS with parameters different for interactions between SPH particles of the same fluids and particles of

different fluids (such as Eqs. (56) and (52)) as “heterogeneous EOS.” EOS with parameters independent of the type of SPH particles will be referred to as “homogeneous EOS.”

The partial surface tension due to  $\mathbf{F}_{ij}^{int}$  is given by

$$\sigma_{\alpha\beta}^{int} = \lambda(n_\alpha^2 s_{\alpha\alpha} + n_\beta^2 s_{\beta\beta} - 2n_\alpha n_\beta s_{\beta\alpha}) = \lambda\bar{\sigma}_{\alpha\beta}, \quad (57)$$

where  $\bar{\sigma}_{\alpha\beta} = \bar{s}_{\alpha\alpha} + \bar{s}_{\beta\beta} - 2\bar{s}_{\beta\alpha}$  and  $\bar{s}_{\beta\alpha} = n_\alpha n_\beta s_{\beta\alpha}$ .

Eqs. (56) and (57) show that the surface tension in the compressible and weakly compressible SPH multiphase models can be generated with only the “pressure gradient” forces (i.e., without the pairwise forces  $\mathbf{F}_{ij}^{int}$ ) by using a heterogeneous EOS. There are several limitations with this approach. The pressure gradient forces may not be sufficient to generate surface tension in free-surface models (i.e. models where only the liquid phase is modeled and the gas phase is disregarded) [28]. In addition, to prescribe the boundary condition (5), one needs to specify heterogeneous EOS at the fluid–solid interface. Most importantly, in weakly compressible SPH, EOS play an important role of controlling fluid compressibility, which limits the freedom of choice of the parameters in an EOS to define the surface tension according to, for example, Eqs. (52) or (56). Finally, this approach cannot be used for modeling incompressible fluids and is only limited to the compressible and weakly compressible SPH models because it requires prescribing a heterogeneous EOS. Because of these limitations, in the PF-SPH method, it is more common to generate surface tension using the pairwise force  $\mathbf{F}_{ij}^{int}$  rather than heterogeneous EOS. In the following, we will use the homogeneous EOS (Eq. (49) with constant  $T$ ) in combination with the  $\mathbf{F}_{ij}^{int}$  forces to generate surface tension. Already, we have demonstrated that for homogeneous EOS,  $\sigma_{\alpha\beta}^P = 0$ . Therefore,

$$\sigma_{\alpha\beta} = \sigma_{\alpha\beta}^{int}. \quad (58)$$

For three fluids resting in contact with each other, the contact angles as a function of the parameters in the pairwise forces can be found from Eqs. (38) and (57):

$$\begin{aligned} \cos\theta_1 &= \frac{\sigma_{23}^2 - \sigma_{13}^2 - \sigma_{12}^2}{2\sigma_{13}\sigma_{12}} = \frac{\bar{\sigma}_{23}^2 - \bar{\sigma}_{13}^2 - \bar{\sigma}_{12}^2}{2\bar{\sigma}_{13}\bar{\sigma}_{12}}, \\ \cos\theta_2 &= \frac{\sigma_{13}^2 - \sigma_{12}^2 - \sigma_{23}^2}{2\sigma_{23}\sigma_{12}} = \frac{\bar{\sigma}_{13}^2 - \bar{\sigma}_{12}^2 - \bar{\sigma}_{23}^2}{2\bar{\sigma}_{23}\bar{\sigma}_{12}}, \\ \cos\theta_3 &= \frac{\sigma_{12}^2 - \sigma_{23}^2 - \sigma_{13}^2}{2\sigma_{23}\sigma_{13}} = \frac{\bar{\sigma}_{12}^2 - \bar{\sigma}_{23}^2 - \bar{\sigma}_{13}^2}{2\bar{\sigma}_{23}\bar{\sigma}_{13}}. \end{aligned} \quad (59)$$

Substituting Eq. (57) into the Young–Laplace equation gives an expression for the static contact angle  $\theta$  as a function of the parameters in the pairwise forces:

$$\cos\theta_0 = \frac{\mathcal{T}_{\beta\beta}^{int} - \mathcal{T}_{\alpha\alpha}^{int} - 2\mathcal{T}_{\beta\alpha}^{int} + 2\mathcal{T}_{\alpha\beta}^{int}}{\mathcal{T}_{\alpha\alpha}^{int} + \mathcal{T}_{\beta\beta}^{int} - 2\mathcal{T}_{\alpha\beta}^{int}} = \frac{\bar{s}_{\beta\beta} - \bar{s}_{\alpha\alpha} - 2\bar{s}_{\beta\alpha} + 2\bar{s}_{\alpha\beta}}{\bar{s}_{\alpha\alpha} + \bar{s}_{\beta\beta} - 2\bar{s}_{\alpha\beta}}. \quad (60)$$

Eqs. (57)–(60) show that the surface tension produced by the PF-SPH model (Eqs. (11) and (12)) depends on the form of  $F_{\alpha\beta}^{int}$ , but the equilibrium contact angles for a three-fluid system and two fluids in contact with a solid depend only on  $s_{\alpha\beta}$  and the number density.

In general, for a given numerical resolution, an infinite combination of parameters  $s_{\alpha\beta}$  can result in the same values of the surface tension and contact angles. In the following, we suggest a model with a reduced number of parameters, which allows a unique parameterization of the SPH model. We also demonstrate that the PF-SPH model produces surface tension and contact angles that are in good agreement with the prescribed surface tension and contact angles.

### 5.3. Parameterization of the PF-SPH model with respect to surface tension and static contact angle

In this section, we present parameterization of the SPH model with respect to the surface tension,  $\sigma_{\alpha\beta}$ , and the static contact angle,  $\theta_0$ .

Eq. (57) shows that for  $\alpha$  and  $\beta$  fluids to be immiscible (i.e., for  $s_{\alpha\beta}$  to be positive), it is sufficient for  $s_{\alpha\beta}$ ,  $s_{\beta\beta}$ , and  $s_{\alpha\alpha}$  to satisfy the condition  $\bar{s}_{\alpha\alpha} + \bar{s}_{\beta\beta} > 2\bar{s}_{\alpha\beta}$ . To reduce the number of parameters and satisfy the preceding condition, we set  $\bar{s}_{\alpha\alpha} = \bar{s}_{\beta\beta} = 10^\kappa \bar{s}_{\alpha\beta}$  with  $\kappa > 1$ . Then, for a fluid–fluid–solid system, Eq. (60) reduces to:

$$\bar{s}_{\alpha\beta} - \bar{s}_{\beta\alpha} = \frac{1}{2} \frac{\sigma_{\alpha\beta}}{\lambda} \cos\theta_0. \quad (61)$$

Next, to define the parameters uniquely, we set  $\bar{s}_{\alpha\beta} = \bar{s}_{\alpha\alpha} - \beta$  and  $\bar{s}_{\beta\alpha} = \bar{s}_{\alpha\alpha} + \beta$  ( $\beta$  is a constant) and assume that: 1) the initial discretization of the  $\alpha$  and  $\beta$  phases is the same (i.e.,  $n_\alpha = n_\beta = n_{eq}$ ); 2) fluids are low compressible and  $n_\alpha$  and  $n_\beta$  can be treated as a constant; and 3)  $10^{-\kappa} \ll 1$  (e.g., in [32],  $\kappa = 4$  was used). Then, the parameters in the PF-SPH model can be related to the surface tension, static contact angle, and SPH discretization parameters  $h$  and  $n$  as:

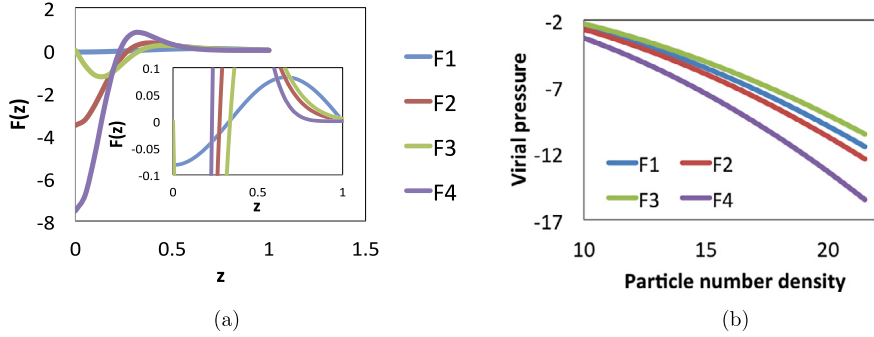


**Fig. 3.** (a)  $F_{k,\alpha\beta}(z)$  ( $k = 1, 2, 3, 4$ ) for the surface tension  $\sigma_{\alpha\beta} = 2$  (in the model units). (b) Virial pressure generated by the forces  $\mathbf{F}_{k,ij} = -F_{k,\alpha\beta}(r_{ij}) \frac{\mathbf{r}_{ij}}{r_{ij}}$  in a bulk fluid (away from the interface) as a function of particle number density  $n$  for  $n_{eq} = 16$ .

**Table 2**

The relative error between the prescribed and resulting surface tension  $|\sigma_{\alpha\beta} - \sigma_{\alpha\beta}^r|/\sigma_{\alpha\beta}$  for different forces  $F_{k,\alpha\beta}^{int}$  ( $k = 1, 2, 3, 4$ ) and particle number densities.

$n_{eq}$	$F_{1,\alpha\beta}^{int}$	$F_{2,\alpha\beta}^{int}$	$F_{3,\alpha\beta}^{int}$	$F_{4,\alpha\beta}^{int}$
9	0.442	0.075	0.004	1.13
16	0.034	0.044	0.026	0.014
25	0.053	0.067	0.071	0.141
36	0.064	0.067	0.068	0.039
49	0.072	0.078	0.069	0.024

$$s_{\alpha\alpha} = s_{\beta\beta} = \frac{1}{2} n_{eq}^{-2} \frac{\sigma_{\alpha\beta}}{\lambda} \quad (62)$$

and

$$s_{s\alpha} = \frac{1}{2} n_{eq}^{-2} \frac{\sigma_{\alpha\beta}}{\lambda} \left( 1 + \frac{1}{2} \cos \theta_0 \right) \quad \text{and} \quad s_{s\beta} = \frac{1}{2} n_{eq}^{-2} \frac{\sigma_{\alpha\beta}}{\lambda} \left( 1 - \frac{1}{2} \cos \theta_0 \right). \quad (63)$$

Similar expressions for  $s_{\alpha\alpha}$ ,  $s_{s\alpha}$ , and  $s_{s\beta}$  have been obtained in Bandara et al. [3] based on Maxwell's theory of the capillarity [18].

The pairwise force  $\mathbf{F}_{ij}^{int} = -F_{\alpha\beta}^{int}(r_{ij}) \frac{\mathbf{r}_{ij}}{r_{ij}}$  with  $F_{\alpha\beta}^{int} = F_{2,\alpha\beta}^{int}$ ,  $F_{3,\alpha\beta}^{int}$ , or  $F_{4,\alpha\beta}^{int}$  in Table 1 has several additional parameters: the parameter  $A$ , defining the relative magnitude of the repulsive and attractive parts of the force; and  $\varepsilon$  and  $\varepsilon_0$  in  $F_{\alpha\beta}^{int} = F_{2,\alpha\beta}^{int}$  and  $F_{3,\alpha\beta}^{int}$  and  $h_0$  in  $F_{4,\alpha\beta}^{int}$ , defining the relative range of the repulsive and attractive parts of the force. Based on physical considerations and by drawing an analogy with intermolecular forces, we conclude that  $\varepsilon_0$  should be smaller than  $\varepsilon$ . Besides that, the parameter values determine distribution of the SPH particles. By construction, the force  $\mathbf{F}_{ij}^{int} = -F_{4,\alpha\beta}(r_{ij}) \frac{\mathbf{r}_{ij}}{r_{ij}}$  has the compact support  $h$ , which requires only neighboring particles within the distance  $h$  from any particle  $i$  to be included in summation in Eq. (12) for  $\mathbf{F}_i^{int}$ . The functions  $F_{2,\alpha\beta}^{int}$  and  $F_{3,\alpha\beta}^{int}$  are a combination of two Gaussian functions with the standard deviations  $\varepsilon_0$  and  $\varepsilon$  ( $\varepsilon_0 < \varepsilon$ ). For computational efficiency (i.e., in Eq. (12) to sum only over particles within the distance  $h$  of particle  $i$ ), one should chose  $\varepsilon < h/3$  for these functions to nearly vanish for  $r_{ij} > h$ . In the following simulations, we set  $\varepsilon = h/3.5$ . The parameter  $A$  in  $F_{2,\alpha\beta}^{int}$ ,  $F_{3,\alpha\beta}^{int}$ , and  $F_{4,\alpha\beta}^{int}$  is selected to generate negative virial pressure. The values of  $A$ ,  $\varepsilon_0/\varepsilon$ , and  $h_0/h$ , used in the simulations, are shown in Table 1. Fig. 3(a) shows  $F_{k,\alpha\beta}(z)$  ( $k = 1, 2, 3, 4$ ) as a function of  $z$ , corresponding to the surface tension  $\sigma_{\alpha\beta} = 2$  (in the model units). All pairwise forces have support  $h = 1$  (in the model units) or decay rapidly for  $z > 1$ . Fig. 3(b) shows the virial pressure generated by these forces as a function of particle density.

To study the effect of the functional form of  $F_{k,\alpha\beta}^{int}(z)$ , and the corresponding parameters on the distribution of the SPH particles, and accuracy of the proposed parameterization of the PF-SPH model, we simulate fluids  $\alpha$  and  $\beta$  separated by a flat interface and a bubble of the fluid  $\alpha$  surrounded by the fluid  $\beta$  in two spatial dimensions using the force  $\mathbf{F}_{ij}^{int}$  with  $F_{k,\alpha\beta}^{int}$  ( $k = 1, 2, 3, 4$ ). In these simulations, the particles are placed randomly in the computational domain by dividing the domain in square subdomains with the size  $h^2$  and randomly placing  $n_{eq}$  particles in each. Then, the simulations proceed as described in Section 4.

From the simulations of two fluids separated by a flat interface, we compute the resulting surface tension  $\sigma_{\alpha\beta}^r$  using Eq. (28). Table 2 gives the relative error between the prescribed and resulting surface tension  $|\sigma_{\alpha\beta} - \sigma_{\alpha\beta}^r|/\sigma_{\alpha\beta}$  for

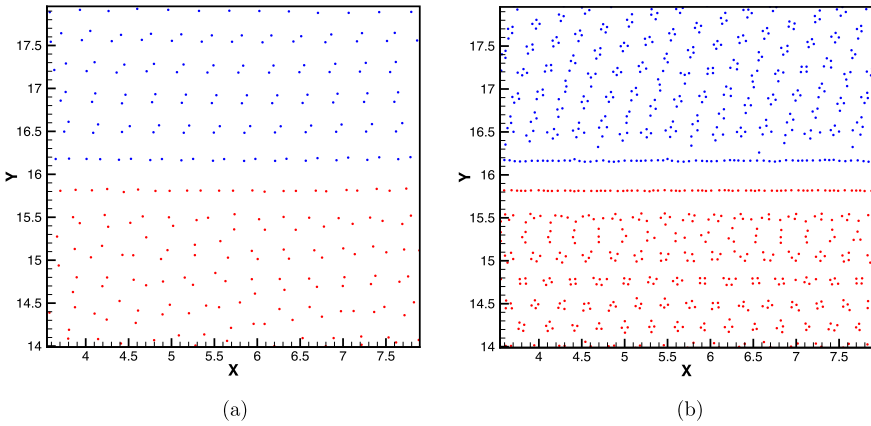


**Fig. 4.** Simulation of two fluids separated by a flat front.  $F_{1,\alpha\beta}^{int}$  with  $\bar{s}_{\alpha\alpha} = 16^2 \times 0.1$  and  $\bar{s}_{\alpha\beta} = 16^2 \times 0.00001$ . (a)  $n_{eq} = 16$  and (b)  $n_{eq} = 49$ .

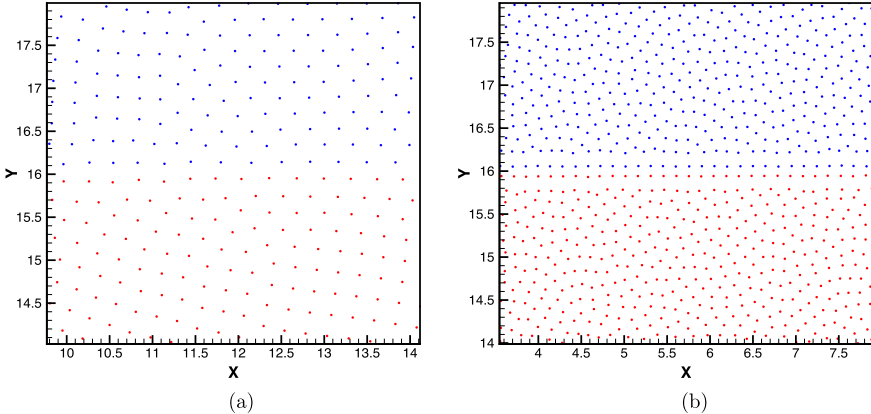


**Fig. 5.** Simulation of two fluids separated by flat front.  $F_{3,\alpha\beta}^{int}$  with  $\tilde{s}_{\alpha\alpha} = 16^2 \times 2$  and  $\tilde{s}_{\alpha\beta} = 16^2 \times 0.00001$ . (a)  $n_{eq} = 16$  and (b)  $n_{eq} = 49$ .

different forces and particle number densities. In most cases, the error is below 10%. For  $n_{eq} = 16$  (commonly used in two-dimensional simulations with the forth-order spline weighting function), the error is less than 5% for all tested  $F_{\alpha\beta}^{int}$ . We can see there is no strong dependence of the error on  $n_{eq}$ . In general, the error in the SPH method should decrease with increasing  $n_{eq}$ . Furthermore, the proposed parameterization of the PF-SPH model is based on an integral approximation of Eq. (26). For uniformly distributed SPH particles, the accuracy of this approximation should increase with increasing  $n_{eq}$ . One possible explanation for the error in Table 2—in some cases, increasing with increasing  $n_{eq}$ —is that for the parameters used in  $F_{\alpha\beta}^{int}$ , the particles become more disordered with increasing  $n_{eq}$ . For example, Fig. 4 shows simulations of two fluids separated by a flat front with the pairwise force  $F_{1,\alpha\beta}^{int}$  at two resolutions,  $n_{eq} = 16$  and 49. In the simulations at both resolutions, some clustering of particles is observed, but the clustering is more pronounced in the simulation with  $n_{eq} = 49$  than  $n_{eq} = 16$ . Fig. 5 shows simulations with the pairwise force  $F_{3,\alpha\beta}^{int}$  and two resolutions,  $n_{eq} = 16$  and 49. Here, particles are uniformly distributed in the simulation with  $n_{eq} = 16$ , but they form a gap near the interface in the simulation with  $n_{eq} = 49$ . It might be possible to improve the particle distribution in the simulation with  $n_{eq} = 49$  by adjusting the ratio  $\varepsilon/\varepsilon_0$ . We have determined that for  $n_{eq} = 16$ , the best results in terms of particle distribution and error are obtained with  $\varepsilon/\varepsilon_0 = 2$  in  $F_{2,\alpha\beta}^{int}$  and  $F_{3,\alpha\beta}^{int}$  and  $h/h_0 = 2$  in  $F_{4,\alpha\beta}^{int}$ .

Some of the simulations of a fluid bubble are shown in Fig. 6. Fig. 6(a) depicts the particle distribution obtained from the simulation with  $F_{1,\alpha\beta}^{\text{int}}$ . Figs. 6(b) and 6(c) show the particle distributions obtained from the simulations with  $F_{3,\alpha\beta}^{\text{int}}$ ,  $A = (\varepsilon_0/\varepsilon)^4$  and  $\varepsilon_0 = 0.5\varepsilon$  and  $\varepsilon_0 = 0.4\varepsilon$ , respectively. It is evident that the pairwise force with  $F_{3,\alpha\beta}^{\text{int}}$  and  $\varepsilon_0 = 0.5\varepsilon$  produces a more uniform distribution of particles than the other two simulations. Similar simulations of the bubble with  $F_{2,\alpha\beta}^{\text{int}}$ ,  $\varepsilon_0 = 0.5\varepsilon$  and  $A = (\varepsilon_0/\varepsilon)^3$ , and  $F_{4,\alpha\beta}^{\text{int}}$ ,  $h_0 = 0.5h$  and  $A = (\varepsilon_0/\varepsilon)^3$ , produced a uniform particle distribution similar to the one shown in Fig. 6(b).

Next, we simulate bubbles of different sizes and demonstrate that the PF-SPH model, with parameters estimated from Eqs. (62) and (63), produces correct surface tension and static contact angle. First, we compute the surface tension using

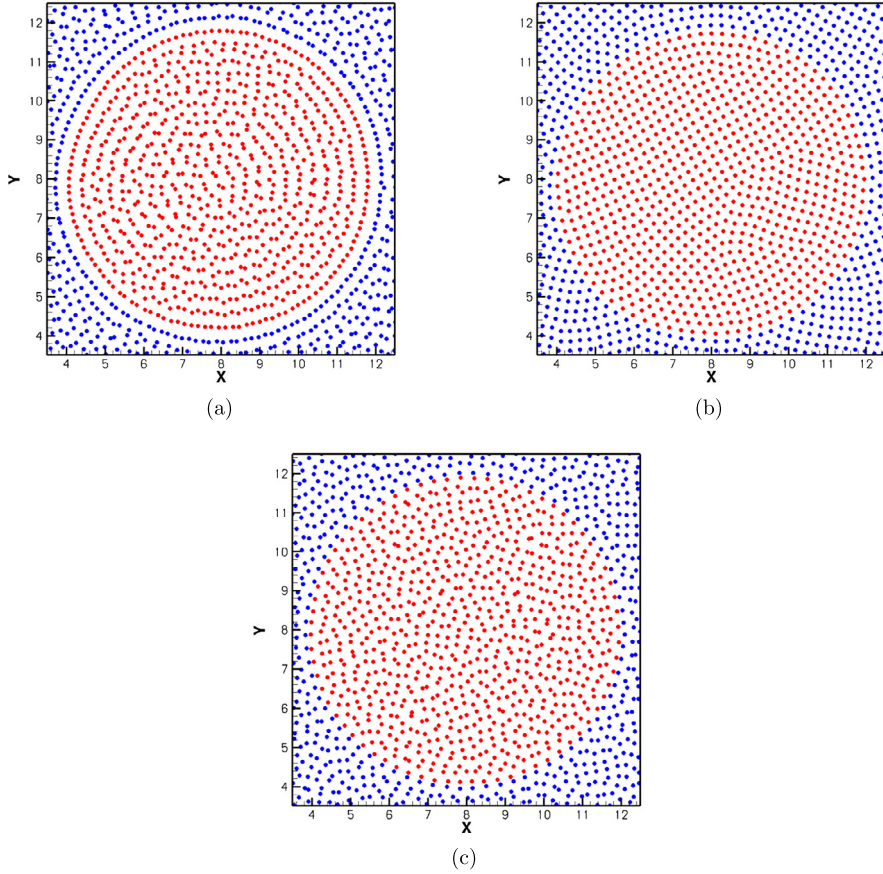


**Fig. 6.** Particle distribution obtained from simulations of a bubble of one fluid surrounded by another fluid with: (a) cosine pairwise force; (b) the pairwise force  $F_{3,\alpha\beta}^{\text{int}}(r_{ij}) = s_{\alpha\beta} r_{ij} [-A\psi_{\varepsilon_0}(r_{ij}) + \psi_{\varepsilon}(r_{ij})]$  with  $\varepsilon_0 = 0.5\varepsilon$ ; and (c)  $F_{3,\alpha\beta}^{\text{int}}(r_{ij})$  with  $\varepsilon_0 = 0.4\varepsilon$ .

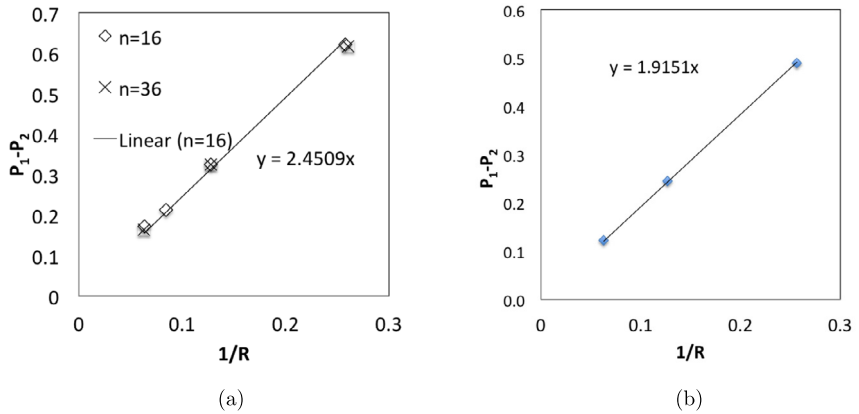


**Fig. 7.**  $P_1 - P_2$  versus  $1/R$  obtained from SPH simulations of a bubble of Fluid 1 with radius  $R$  surrounded by Fluid 2. The results are obtained with: (a) cosine pairwise function with the parameters  $\tilde{s}_{11} = \tilde{s}_{22} = 16^2 \times 0.1$  and  $\tilde{s}_{12} = 16^2 \times 0.00001$ ; and (b)  $F_{3,\alpha\beta}^{\text{int}}(r_{ij})$  pairwise force with parameters  $\tilde{s}_{11} = \tilde{s}_{22} = 16^2 \times 2$ , and  $\tilde{s}_{12} = 16^2 \times 0.00001$ ,  $\varepsilon = h/3.5$ ,  $\varepsilon_0 = \varepsilon/2$ , and  $A = \varepsilon^3/\varepsilon_0^3$ . In (a), a good agreement is observed between results obtained with  $n = 16$  and  $36$ . The surface tension, found from a linear regression analysis, is  $2.45$ , agreeing well (within 1%) with the value  $\sigma = 2.43$  predicted by Eq. (57). In (b), the surface tension, found from a linear regression analysis, is  $1.91$ , within 5% agreement with the value  $\sigma = 1.83$  predicted by Eq. (57).

the pressures inside and outside of the bubble and radius of the bubble at the equilibrium,  $R$ , using the Young–Laplace law

$$P_1 - P_2 = \frac{\sigma}{R}, \quad (64)$$

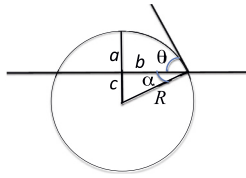


**Fig. 8.** Sketch of a droplet (the segment of the circle above the horizontal line) on the flat surface (the horizontal line). Contact angle  $\theta$  is determined from the height  $a$  of the droplet and the lateral size  $2b$ .

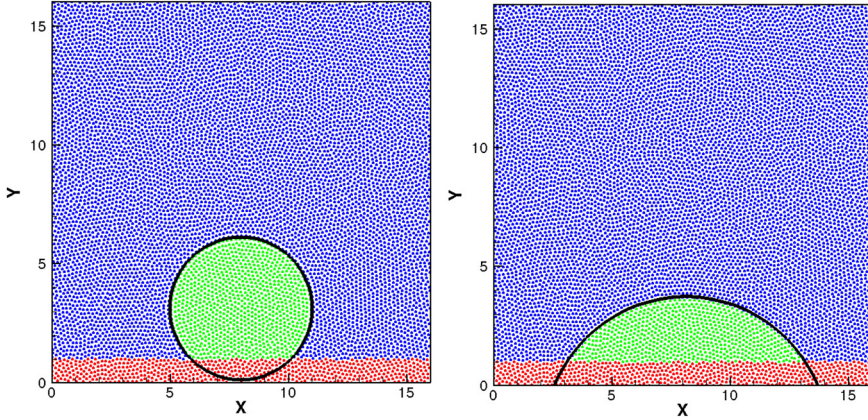


**Fig. 9.** Simulations of a bubble on a solid wall with  $F_{3,\alpha\beta}^{int}$ . The surface tension between two fluids is  $\sigma = 1.83$  in model units. Left figure: Bubble of a non-wetting fluid on a flat surface surrounded by a wetting fluid in the absence of gravity. Prescribed and simulated static contact angles are  $\theta = 2.34$  and  $2.35$  rad, correspondingly. Right figure: Bubble of a wetting fluid on a flat surface surrounded by a non-wetting fluid in the absence of gravity. Prescribed and simulated static contact angles are  $\theta = 1.04$  and  $0.99$  rad, correspondingly. In both these figures, the black circle is fitted to the simulated droplet to demonstrate that in the absence of gravity, the droplet forms a segment of a circle. These simulations are performed with particle number density  $n = 36$ .

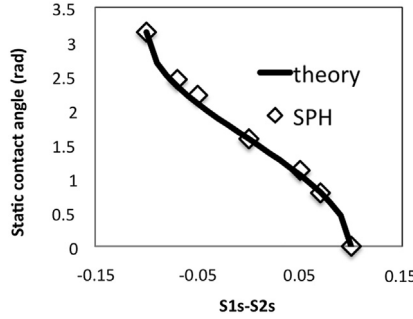
where  $P_1$  and  $P_2$  are the fluid pressures inside and outside of the bubble and  $\sigma$  is the surface tension. Figs. 7(a) and (b) show  $P_1 - P_2$  versus  $1/R$  obtained from the simulations with  $F_{1,\alpha\beta}^{int}$  and  $F_{3,\alpha\beta}^{int}$ , respectively. These figures demonstrate that  $P_1 - P_2$  varies linearly as a function of  $1/R$ . According to the Young–Laplace law, we compute the surface tension as the slope of the lines formed by the  $P_1 - P_2$  versus  $1/R$  data. For the considered parameters (listed in the caption of Fig. 7), the surface tension, found from the SPH simulations, are within 5% of the value predicted by Eq. (57). The simulations with  $F_{1,\alpha\beta}^{int}$  are conducted at two different resolutions (particle number densities  $n$ ), and Fig. 7(a) shows that the results of the SPH simulations—hence, the accuracy of Eq. (57)—are practically independent of the resolution. We also computed the surface tension from the “bubble” simulations using Eq. (28) and found it to closely agree with the surface tension determined with the Young–Laplace formula.

Next, we demonstrate that the static contact angle, obtained in the SPH model, agrees with Eq. (60). We simulate a droplet of Fluid 1 in contact with the solid surface and surrounded by Fluid 2. We start with a droplet, forming the contact angle  $\pi/2$  with the solid surface, and let the droplet relax to an equilibrium with the solid and surrounding fluid. The accurate direct measurement of the contact angle from a simulated droplet can be complicated. Instead, we measure the droplet’s height,  $a$ , and width,  $2b$  (see Fig. 8), and calculate the static contact angle as:

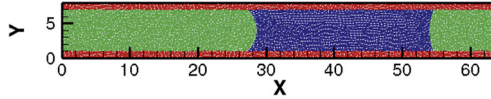
$$\theta = \frac{\pi}{2} - \text{Arcsin} \left[ \frac{b^2 - a^2}{b^2 + a^2} \right]. \quad (65)$$

Fig. 9 depicts the results of numerical simulations with  $\theta_0 = 2.34$  and  $1.04$  rad with  $F_{3,\alpha\beta}^{int}$  and  $n_{eq} = 36$ . For  $\theta_0 = 2.34$ , the difference between prescribed and resulting static contact angles is 1%. For  $\theta_0 = 1.04$ , the error is 5%. Simulations with  $n_{eq} = 16$  have produced results with similar errors. The same simulations with  $F_{1,\alpha\beta}^{int}$  have resulted in  $\approx 5\%$  errors for  $n_{eq} = 36$ , but significantly larger errors (up to 30%, depending on the prescribed static contact angle) for  $n_{eq} = 16$ . The reason for the higher accuracy of the simulations with  $F_{3,\alpha\beta}^{int}$  relative to the simulations with  $F_{1,\alpha\beta}^{int}$  is a more uniform distribution of SPH particles in the former than the latter. For example, Fig. 6 shows the effect of the form of  $F_{k,\alpha\beta}^{int}$  on the particle distribution. Fig. 10 shows the static contact angle  $\theta_0$  as a function of  $\bar{s}_{1s} - \bar{s}_{2s}$ , obtained from the PF-SPH simulations with  $F_{3,\alpha\beta}^{int}$  and  $n_{eq} = 36$  and calculated from Eq. (60). Good agreement (within 5%) between the SPH results and the analytical expression is observed for the entire range of static contact angles ( $\theta_0$ , varying from 0 to  $\pi$ ).

Next, we demonstrate the accuracy of the PF-SPH model under dynamic conditions. To do this, we simulate the flow of a droplet of a wetting fluid between two parallel plates, driven by a body force. The simulation setup is shown in Fig. 11.



**Fig. 10.** The contact angle versus  $\bar{s}_{1s} - \bar{s}_{2s}$  formed between Fluids 1 and 2 and the solid phase  $s$ . The solid line is the angle obtained from Eq. (60), and the symbols represent the contact angles obtained from the SPH simulations.  $\bar{s}_{11} = \bar{s}_{22} = 16^2 \times 0.1$ ,  $\bar{s}_{12} = 16^2 \times 0.00001$ , and  $n = 36$ .



**Fig. 11.** Simulation of a droplet flow between two parallel plates under the influence of the body force acting from left to right. In this simulation,  $n_{eq} = 36$ , density and viscosity of the liquid (Fluid 1 denoted by blue particles) are  $\rho_l = 36$  and  $\mu_l = 1$ . Density and viscosity of the gas (Fluid 2 denoted by green particles) are  $\rho_g = 0.0036$  and  $\mu_g = 0.001$ . The surface tension and static contact angle are  $\sigma = 1.83$  and  $\theta_0 = 1.069$  rad. The body force per unit mass is  $g = 0.00089$ , resulting in  $Ca = \frac{u\mu_l}{\sigma} = 0.036$ , where  $u$  is the steady-state velocity of the droplet. The pairwise force is  $F_{3,\alpha\beta}^{int}(r_{ij}) = s_{\alpha\beta}r_{ij}[-A\psi_{\varepsilon_0}(r_{ij}) + \psi_{\varepsilon}(r_{ij})]$  with  $\varepsilon = h/3.5$ ,  $\varepsilon_0 = \varepsilon/2$ ; and  $s_{11} = s_{22} = 0.395$ ,  $s_{12} = s_{11} \times 10^{-5}$ ,  $s_{1s} = 1.24s_{11}$ , and  $s_{2s} = 0.76s_{11}$ . (For interpretation of the references to color in this figure, the reader is referred to the web version of this article.)

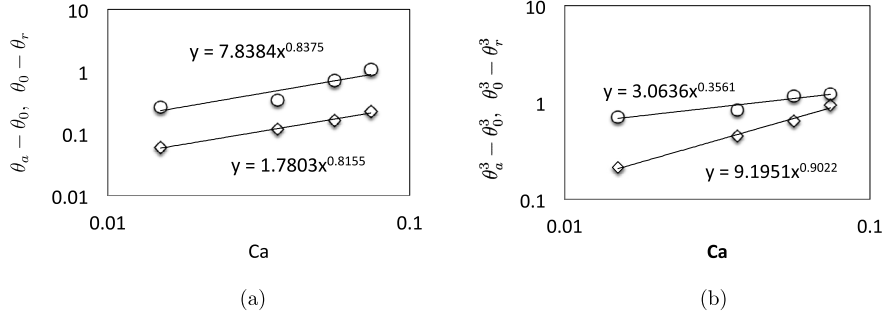


**Fig. 12.** Left panel:  $\theta_a - \theta_0$  (diamonds) and  $\theta_0 - \theta_r$  (circles) versus  $Ca$  obtained from the simulations of a droplet flowing between two parallel plates. Right panel:  $\theta_a^3 - \theta_0^3$  (diamonds) and  $\theta_0^3 - \theta_r^3$  (circles) versus  $Ca$  obtained from the same simulations. Here  $\theta_a$ ,  $\theta_r$ , and  $\theta_0$  are the advancing, receding, and static contact angles formed by the bubble surface and the planes. The setup and parameters of the simulations are given in Fig. 11. In the simulations, the capillary number is changed by altering  $g$ , the body force per unit length. Power law fit to the data also is shown.

The steady-state droplet's velocity,  $u$ , can be related to the surface tension and the receding ( $\theta_r$ ) and advancing ( $\theta_a$ ) contact angles via the analytical expression [8]:

$$u = \frac{b^2}{12\mu} \left[ \rho g + \frac{\sigma}{L} \left( \frac{1}{R_a} - \frac{1}{R_r} \right) \right], \quad (66)$$

where  $L$  is the length of the droplet,  $b$  is the distance between the two plates and  $R_a$ , and  $R_r$  are the radii of the curvatures formed by the receding and advancing contact angles. We conduct four simulations with capillary numbers  $Ca = \frac{u\mu}{\sigma} = 0.074, 0.056, 0.036$ , and  $0.0015$ . The difference between  $u$  found from the simulations and Eq. (66) for all considered  $Ca$  is less than 7%. Fig. 12(a) shows the receding and advancing contact angles as functions of  $Ca$  obtained from the SPH simulations. It demonstrates that the receding and advancing dynamic contact angles follow the power law described by Eq. (6). Fig. 12(b) shows  $\theta_a^3 - \theta_0^3$  and  $\theta_0^3 - \theta_r^3$  as functions of  $Ca$ . It can be seen that  $\theta_a^3 - \theta_0^3$  scales as  $Ca^{0.9}$ , which agrees well with the Cox-Voinov relationship for the advancing contact angle  $\theta_a^3 - \theta_0^3 = a_a Ca$  ( $a_a$  is the parameter related to microscopic properties of the interface) [6].

Under certain conditions, e.g., withdrawing the plate from a bath of liquid, it has been shown that the Cox-Voinov relationship also holds for receding contact angles, i.e.,  $\theta_0^3 - \theta_r^3 = a_r Ca$  ( $a_r$  is the parameter related to microscopic properties of the interface) [4]. Fig. 12(b) shows that for a bubble moving between two parallel walls, the receding contact angle does not satisfy the Cox-Voinov relationship. To show that the Cox-Voinov relationship cannot hold for both the receding and advancing contact angles of the bubble, we can rewrite Eq. (66) as  $\cos \theta_r - \cos \theta_a = Ca \left[ \frac{6L}{b} - \frac{bL\rho g}{2\mu u} \right]$ . On the other hand, the Cox law implies that  $\cos \theta_r - \cos \theta_a \approx a Ca$ , where  $a$  is the velocity independent constant and the relationships

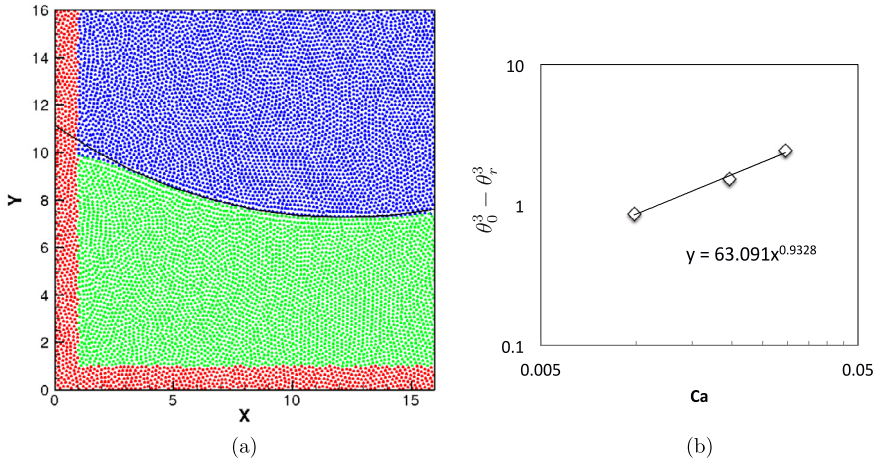


**Fig. 13.** Left panel: Steady-state distribution of fluid phases obtained from a simulation of the withdrawal of a plate from the bath of liquid (Fluid 1 denoted by green particles). Blue particles represent the gas phase (Fluid 2). Red particles represent the solid phase. Zero velocity is imposed at the bottom fluid-solid interface, and the constant velocity vector  $[0, u]^T$  ( $u$  is the velocity of the withdrawing plate) is prescribed at the left fluid-solid vertical boundary. The upper horizontal and right-hand side vertical boundaries are assumed to be impermeable (zero normal velocity) and have zero normal viscous stress. The black line is a part of the circle fitted to the fluid-fluid interface. In this simulation,  $n_{eq} = 36$ ; density and viscosity of the liquid are  $\rho_l = 36$  and  $\mu_l = 3$ , respectively; and density and viscosity of the gas are  $\rho_g = 0.0036$  and  $\mu_g = 0.03$ , respectively. The surface tension and static contact angle are  $\sigma = 1.83$  and  $\theta_0 = \pi/2$ , and the capillary number  $Ca = \frac{u\mu_l}{\sigma} = 0.03$ . The pairwise force is  $F_{3,\alpha\beta}^{int}(r_{ij}) = s_{\alpha\beta}r_{ij}[-A\psi_{\varepsilon_0}(r_{ij}) + \psi_\varepsilon(r_{ij})]$  with  $\varepsilon = h/3.5$ ,  $\varepsilon_0 = \varepsilon/2$ ; and  $s_{11} = s_{22} = s_{15} = s_{25} = 0.395$ , and  $s_{12} = s_{11} \times 10^{-5}$ . Right panel:  $\theta_0^3 - \theta_r^3$  versus  $Ca$ , obtained from the simulations of the plate withdrawal from a bath of liquid. In the simulations, the capillary number is changed by altering  $u$ . Power law fit to the data also is shown. (For interpretation of the references to color in this figure, the reader is referred to the web version of this article.)

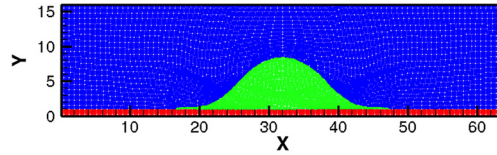


**Fig. 14.** Simulation of a droplet spreading on a horizontal surface under the influence of fluid–solid interactions and surface tension. Green liquid (Fluid 1) is assumed to be fully wetting ( $\theta_0 = 0$ ), and gravity is set to zero. In this simulation,  $n_{eq} = 36$ ; density and viscosity of the liquid are  $\rho_l = 36$  and  $\mu_l = 1000$ , respectively; and density and viscosity of the gas (Fluid 2 represented by blue particles) are  $\rho_g = 0.0036$  and  $\mu_g = 1$ , respectively. The surface tension and static contact angle are  $\sigma = 183$  and  $\theta_0 = 0$  rad. The pairwise force is  $F_{3,\alpha\beta}^{int}(r_{ij}) = s_{\alpha\beta}r_{ij}[-A\psi_{\varepsilon_0}(r_{ij}) + \psi_\varepsilon(r_{ij})]$  with  $\varepsilon = h/3.5$ ,  $\varepsilon_0 = \varepsilon/2$ ; and  $s_{11} = s_{22} = 39.5$ ,  $s_{12} = s_{11} \times 10^{-5}$ ,  $s_{1s} = 1.75s_{11}$ , and  $s_{2s} = 0.25s_{11}$ . (For interpretation of the references to color in this figure, the reader is referred to the web version of this article.)

$\cos \theta_r - \cos \theta_0 \approx 5.63(\theta_0^3 - \theta_r^3)$  and  $\cos \theta_0 - \cos \theta_a \approx 5.63(\theta_a^3 - \theta_0^3)$  for  $|\cos \theta| < 0.65$  are used [26]. To verify that under proper conditions the PF-SPH model can reproduce the Cox–Voinov relationship, we simulate the withdrawal of a plate from the liquid bath. The simulation setup is shown in Fig. 13(a), and the receding angle is computed at the angle formed by a circle, fitted to the interface as shown in the figure, and the solid boundary. Fig. 13(b) demonstrates that the receding contact angle in this problem satisfies the Cox law, i.e.,  $\theta_0^3 - \theta_r^3 \sim Ca^\alpha$  with  $\alpha = 0.93$ , which is close to the theoretical value  $\alpha = 1$ .

Finally, we model the spreading of a droplet on the horizontal surface (Fig. 14) and validate the model by comparing the height of the bubble  $H$  as a function of time with Tanner's law  $H \sim t^{-1/\alpha}$  [27]. The simulation is initialized by placing a droplet of the fully wetting fluid ( $\theta_0 = 0$ ) in the shape of a half circle with radius  $8h$  on the horizontal surface. The rest of the domain is occupied by the non-wetting fluid that has a density 1000 times smaller and viscosity 100 times smaller than the wetting fluid. Tanner has analytically demonstrated that for a two-dimensional bubble formed by a wetting fluid, the exponent is equal to  $\alpha = 7$ . Fig. 15 shows good agreement between  $H$ , as a function of time, found from the simulation and Tanner's law.

#### 5.4. Parameterization of the PF-SPH model for three (or more) fluid phases

For a three-fluid system (e.g., Fluid 1, Fluid 2, and Fluid 3), the surface tensions for each pair of fluids (i.e.,  $\sigma_{12}$ ,  $\sigma_{23}$ , and  $\sigma_{13}$ ) should be specified. For the three fluids to stay in contact with each other at equilibrium, the surface tensions should satisfy the following condition:

$$\begin{aligned} \sigma_{12} &< \sigma_{13} + \sigma_{23} \\ \sigma_{13} &< \sigma_{12} + \sigma_{23} \\ \sigma_{23} &< \sigma_{13} + \sigma_{12} \end{aligned} \tag{67}$$

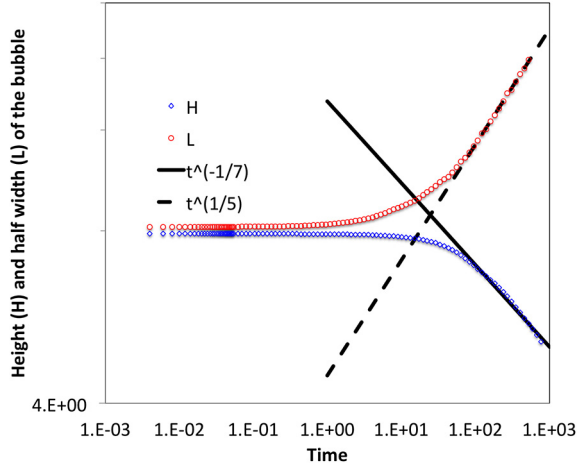


**Fig. 15.** Height of the droplet  $H$  (blue symbols), measured at the center of the drop, and the half-length  $L$  (red symbols), measured from the center to the tip of the advancing film as function of time. The setup and parameters of this simulation are described in Fig. 14. Power law fit to the data also is shown. (For interpretation of the references to color in this figure, the reader is referred to the web version of this article.)

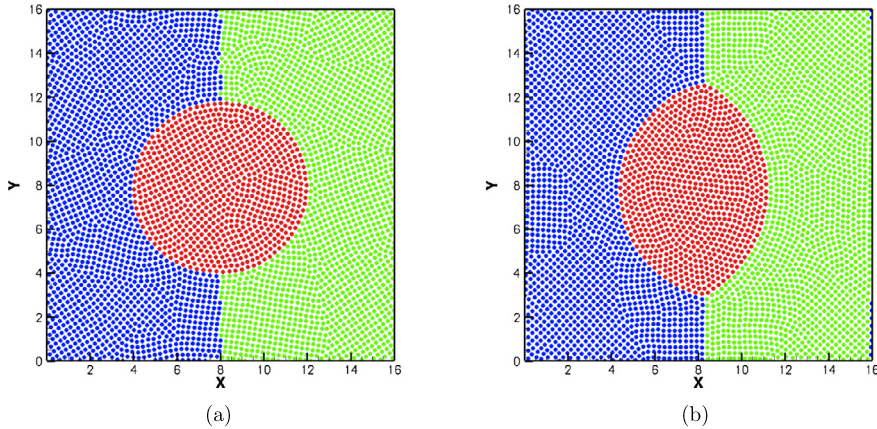


**Fig. 16.** (a) Initial distribution of Fluid 1 (blue fluid), Fluid 2 (green), and Fluid 3 (red); (b) equilibrium distribution of the three fluid phases. The pairwise force is given by  $F_{3,\alpha\beta}^{\text{int}}(r_{ij})$  with  $\varepsilon = h/3.5$  and  $\varepsilon_0 = \varepsilon/2$ ,  $s_{11} = 16^2 \times 2$ ,  $s_{22} = 16^2 \times 3$ ,  $s_{33} = 16^2 \times 4$ ,  $s_{12} = s_{13} = s_{23} = 16^2 \times 0.00001$ . Theory predicts equilibrium contact angles  $\theta_1 = 1.83$ ,  $\theta_2 = 1.97$ , and  $\theta_3 = 2.48$ . The angles measured at the equilibrium from the simulation are  $\theta_1 = 1.77$ ,  $\theta_2 = 1.14$ , and  $\theta_3 = 2.36$ . (For interpretation of the references to color in this figure, the reader is referred to the web version of this article.)

In the PF-SPH model for this type of three-fluid systems, six parameters must be specified:  $s_{11}$ ,  $s_{22}$ ,  $s_{33}$ ,  $s_{12}$ ,  $s_{13}$ , and  $s_{23}$ . To satisfy the conditions (67) and to uniquely define the parameters  $s_{\alpha\beta}$ , it is sufficient to set:

$$s_{\alpha\beta} \ll s_{\alpha\alpha}, \quad \alpha \neq \beta, \quad \alpha, \beta = 1, 2, 3 \quad (s_{\alpha\beta} = s_{\beta\alpha}). \quad (68)$$

Then, from Eq. (57):

$$\begin{aligned} s_{12} &\approx \lambda n_{eq}^2 (s_{11} + s_{22}) \\ s_{13} &\approx \lambda n_{eq}^2 (s_{11} + s_{33}) \\ s_{23} &\approx \lambda n_{eq}^2 (s_{22} + s_{33}). \end{aligned} \quad (69)$$

It can be seen that for any choice of  $s_{\alpha\alpha}$  ( $\alpha = 1, 2, 3$ ), the surface tensions, defined according to Eq. (69), will satisfy the condition (67). The parameters  $s_{\alpha\alpha}$  can be uniquely related to the surface tension by solving the system of equations (69). Fig. 16(b) shows the equilibrium distribution of three fluids obtained with  $s_{11} = 2$ ,  $s_{22} = 3$ ,  $s_{33} = 4$ , and  $s_{12} = s_{13} = s_{23} = 10^{-5}s_{11}$ . In this figure, Fluid 1 is modeled with blue particles, Fluid 2 with green particles, and Fluid 3 with red particles. Fig. 16(a) shows the initial distribution of the fluid phases in this simulation. The contact angles measured at the equilibrium are  $\theta_1 = 1.77$ ,  $\theta_2 = 2.14$ , and  $\theta_3 = 2.36$ . Theory (Eqs. (57) and (59)) predicts equilibrium contact angles  $\theta_1 = 1.83$ ,  $\theta_2 = 1.97$ , and  $\theta_3 = 2.48$ . The difference between prescribed and estimated contact angles is less than 8%.

In the simulations shown in Figs. 17(c)–(d), the parameters  $s_{\alpha\beta}$  ( $\alpha, \beta = 1, 2, 3$ ) are selected to violate the condition (67) (which should prevent all three fluids from staying in contact with each other). In Fig. 17(c), we set  $s_{12} = s_{23} = 0$  ( $s_{\alpha\alpha}$ )

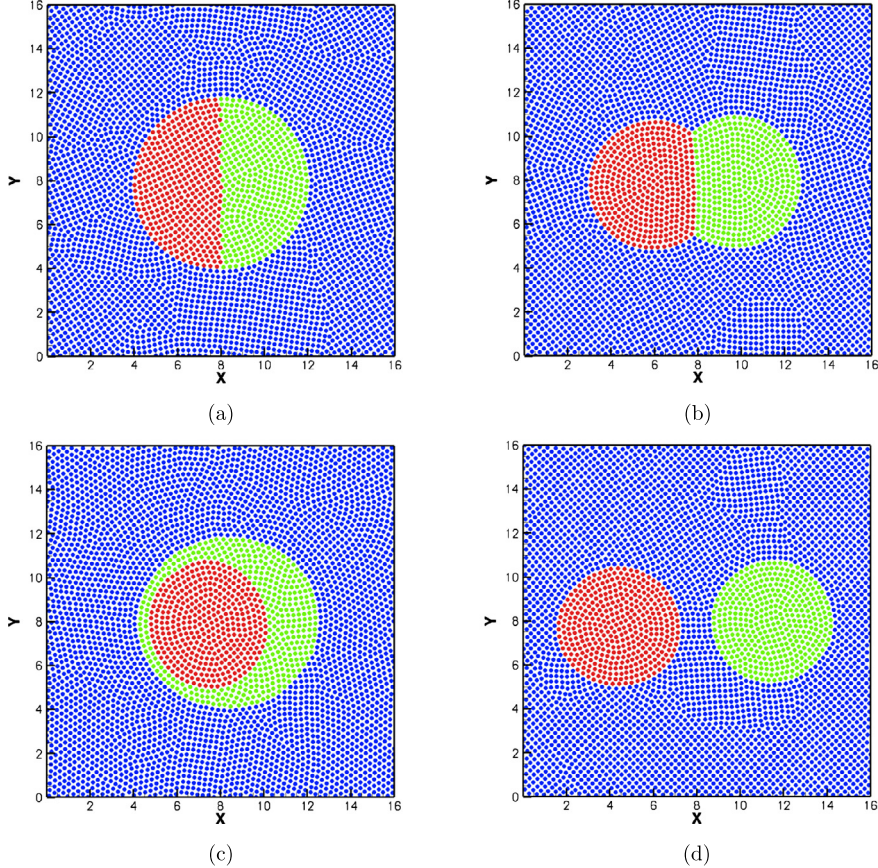


**Fig. 17.** Panel (a): initial distribution of Fluid 1 (blue fluid), Fluid 2 (green), and Fluid 3 (red). Equilibrium distribution of the three fluid phases for the pairwise force  $F_{3,\alpha\beta}^{\text{int}}(r_{ij})$  with: (b)  $\bar{s}_{11} = 16^2 \times 2$ ,  $\bar{s}_{22} = 16^2 \times 3$ ,  $\bar{s}_{33} = 16^2 \times 4$ ,  $\bar{s}_{12} = \bar{s}_{23} = 16^2 \times 0.00001$  and  $\bar{s}_{13} = 16^2 \times 1$ ; (c)  $\bar{s}_{11} = 16^2 \times 4$ ,  $\bar{s}_{22} = 16^2 \times 2$ ,  $\bar{s}_{33} = 16^2 \times 4$ ,  $\bar{s}_{12} = \bar{s}_{23} = 16^2 \times 1.5$ , and  $\bar{s}_{13} = 16^2 \times 0.00001$ ; and (d)  $\bar{s}_{11} = 16^2 \times 2$ ,  $\bar{s}_{22} = 16^2 \times 4$ ,  $\bar{s}_{33} = 16^2 \times 4$ ,  $\bar{s}_{12} = \bar{s}_{13} = 16^2 \times 1.5$ , and  $\bar{s}_{23} = 16^2 \times 0.00001$ . In all simulations  $\varepsilon = h/3.5$  and  $\varepsilon_0 = \varepsilon/2$ . (For interpretation of the references to color in this figure, the reader is referred to the web version of this article.)

and  $s_{13} \ll s_{\alpha\alpha}$ , and in Fig. 17(d), we set  $s_{12} = s_{13} = O(s_{\alpha\alpha})$  and  $s_{23} \ll s_{\alpha\alpha}$ . Fig. 17(a) illustrates the initial distribution of fluid phases. For the same initial configuration of three fluids, we demonstrate in Fig. 17(b) that the fluids are able to stay in contact with each other when Eq. (67) is satisfied. In Figs. 17(c) and 17(d), the condition (67) is not satisfied, and a three-fluid contact line (point in two spatial dimensions) cannot be formed. The parameters used in these simulations are described in the caption for Fig. 17.

## 6. Three-phase flow in porous media

To demonstrate the capabilities and robustness of the PF-SPH method, we use it to simulate three-phase flow in a two-dimensional porous medium, made of irregularly shaped unconnected immobile solid objects, shown in Fig. 18. The porous medium is periodic in the horizontal ( $x$ ) direction and initially filled with Liquid 1. The top and bottom of the porous medium are connected to the atmosphere (i.e., the pressures at top and bottom boundaries are equal). At time zero, Liquid 1 is drained from the porous medium under gravity, acting in the vertical ( $y$ ) direction, and gas (air) enters the pore spaces no-longer occupied by Liquid 1. The equilibrium distribution of Liquid 1 and air is shown in Fig. 18. Here, Liquid 1 is assumed to wet the solid phase in the presence of air. Next, we consider three scenarios where Liquid 2 is injected in the domain through the upper boundary. In the remainder of this section, we use the following notation: the subscripts 1, 2, g, and s denote Liquid 1, Liquid 2, gas, and solid phases, respectively. In Scenario 1, we set  $\sigma_{12} = \sigma_{1g} = \sigma_{2g} = 3.4$  and assume that Liquid 1 wets the solid in the presence of gas and Liquid 2 by setting the static contact angle at the solid boundary formed by Liquid 1 and gas to  $\theta_0^{1g} = 0$  rad, by Liquid 2 and gas to  $\theta_0^{2g} = 0$  rad, and by Liquid 1 and Liquid 2 to  $\theta_0^{12} = 1$  rad. Liquids 1 and 2 and gas are assumed to be able to stay in contact with each other at the equilibrium and form angles  $\theta_1 = \theta_2 = \theta_g = 2.09$ . The second scenario is similar to the first scenario except Liquid 2 wets the solid in the presence of Liquid 1. The static contact angle at the solid boundary formed by Liquid 1 and Liquid 2 is set to  $\theta_0^{1g} = \pi$  rad. The rest of the parameters are the same as in the first scenario. In the third scenario, the wetting behavior is the same as in the

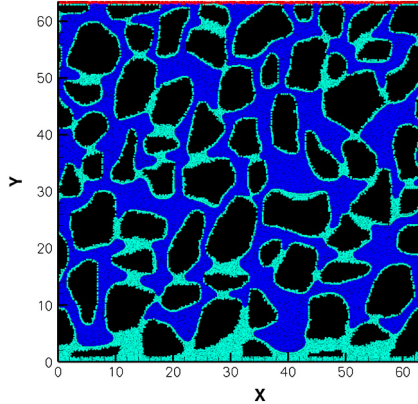


**Fig. 18.** Initial distribution of Fluid 1 (blue fluid), Fluid 2 (green), and Fluid 3 (red). (For interpretation of the references to color in this figure, the reader is referred to the web version of this article.)

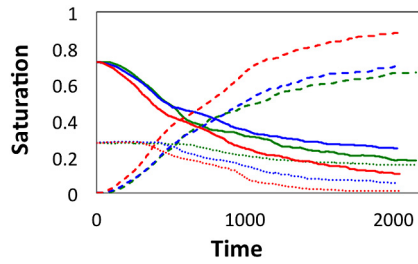


**Fig. 19.** Saturations of three fluids obtained in Cases 1–3.

second scenario, but it is assumed that the three fluids (Liquid 1, Liquid 2, and air) cannot stay in contact with each other. Here, we set  $\sigma_{12} = 1.71$ ,  $\sigma_{1g} = 5.15$ ,  $\sigma_{2g} = 2.58$ ,  $\theta_0^{1g} = 0$  rad,  $\theta_0^{2g} = 0$  rad,  $\theta_0^{12} = \pi$  rad,  $\theta_1 = \pi$ ,  $\theta_2 = 0$ , and  $\theta_g = \pi$ .

Fig. 19 shows the saturations of the three fluids as functions of time observed in the three scenarios. The saturations are greatly affected by the properties of Liquid 2 (properties of Liquid 1 and air stay constant in Scenarios 1 and 2 and change only slightly in Scenario 3). The residual (late time) saturation of Liquid 1 is greatest in Scenario 1 (where Liquid 1 is wetting in presence of Liquid 2 and the surface tension between Liquids 1 and 2,  $\sigma_{12}$ , is relatively large) and the smallest in Scenario 3 (where Liquid 2 is wetting in presence of Liquid 1 and  $\sigma_{12}$  is relatively small). In all three scenarios, the saturation of Liquid 1 starts rapidly decreasing around time  $t = 500$  (in the model units). Fig. 20 shows the distribution of fluid phases in Scenarios 1–3 at the time  $t = 500$  and the late time ( $t = 2020$ ), when the fluids reached a near-equilibrium distribution. In Scenarios 1 and 2, the surface tensions satisfy Eq. (67), i.e., the three fluids should be able to stay in contact with each other at equilibrium. Figs. 20(a), (b), (d), and (e) show that in these scenarios, the displaced fluids (Liquid 1 (green) and air (blue)) stay mostly in contact with each other. Opposite to this, in Scenario 3, we can see many bubbles of the displaced air and Liquid 1 completely surrounded by Liquid 2 (the displacing fluid).

## 7. Conclusions

We presented a new formulation of the Pairwise Force Smoothed Particle Hydrodynamics (PF-SPH) model. In the PF-SPH model, the Young-Laplace and Young boundary conditions at the fluid-fluid and fluid-fluid-solid interfaces are replaced with pairwise forces  $\mathbf{F}_{ij}^{\text{int}} = -F_{\alpha\beta}^{\text{int}}(r_{ij}) \frac{\mathbf{r}_{ij}}{r_{ij}}$ , which are added into the SPH momentum conservation equation. We derived new approximate relationships between the parameters in  $F_{\alpha\beta}^{\text{int}}$  and macroscopic properties of a multiphase flow system. For two fluids in contact with a solid surface, the proposed relationships express the parameters in  $F_{\alpha\beta}^{\text{int}}$  as a function of the surface tension and static contact angle. For a system of three (or more) fluids in which the fluids are able to stay in contact with each other at equilibrium, the parameters in the forces also depend on the equilibrium contact angles formed by any three fluids. We studied the effect of a functional form of  $F_{\alpha\beta}^{\text{int}}$  on the distribution of the SPH particles and the accuracy of the proposed parameterization. We considered four forms of  $F_{\alpha\beta}^{\text{int}}$ , which are listed in Table 1, and demonstrated that  $F_{\alpha\beta}^{\text{int}} = F_{1,\alpha\beta}^{\text{int}}$  leads to clumping of the SPH particles, while the other three forms of  $F_{\alpha\beta}^{\text{int}}$  produce uniform distributions of the particles. The accuracy of SPH discretization schemes decreases as particles become disordered (and clumped together). Therefore, the choice of  $F_{\alpha\beta}^{\text{int}}$  can affect the SPH model's accuracy.

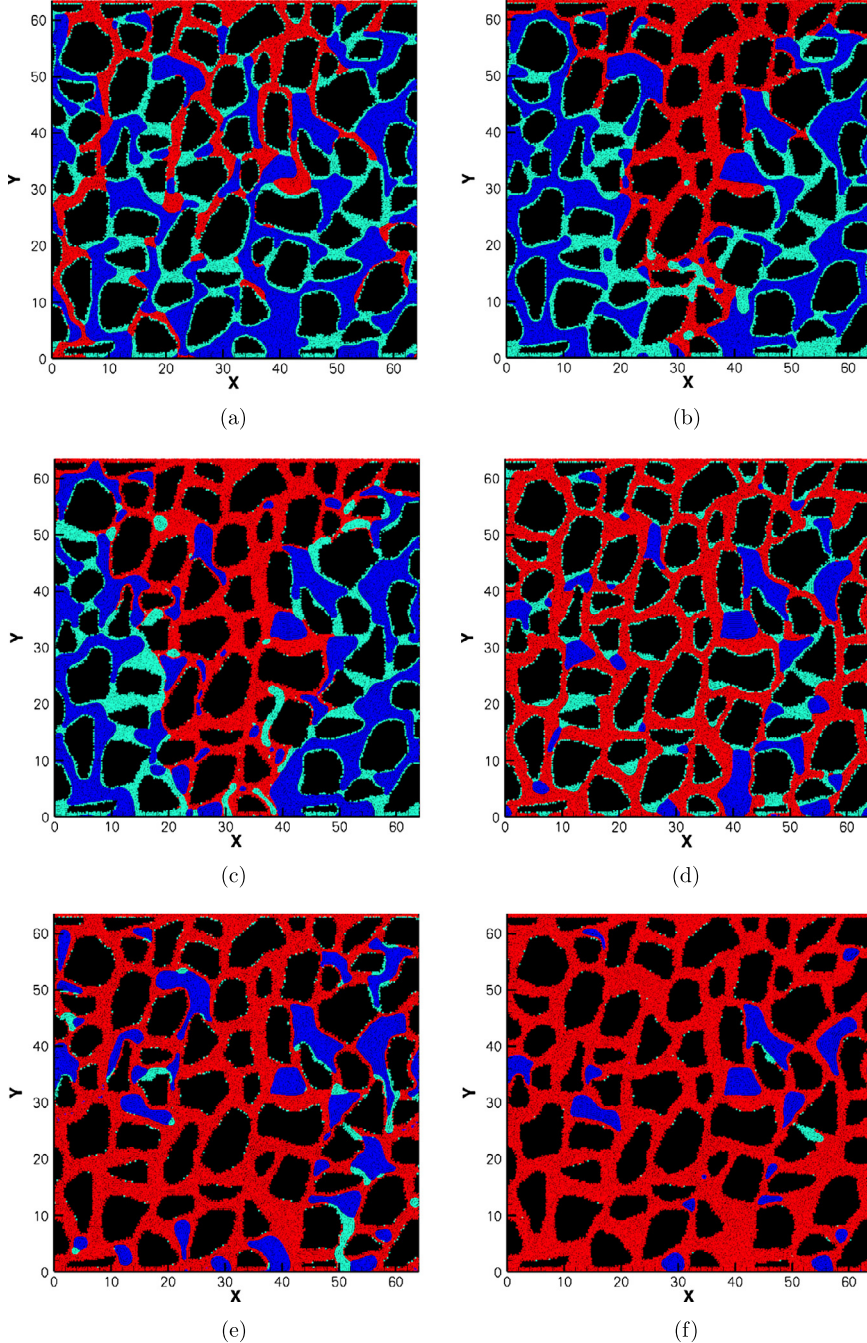


**Fig. 20.** Distribution of Liquid 1 (green), Liquid 2 (red), and air (blue) at different times obtained from Scenarios 1–3. Panels (a) and (d): distribution of the fluid phases at time = 500 and 2020, respectively. Panels (b) and (e): distribution of the fluid phases at time = 500 and 2020, respectively. Panels (c) and (f): distribution of the fluid phases at time = 500 and 2020, respectively. In all simulations,  $n_{eq} = 19$ . Scenario 1:  $s_{11} = s_{22} = s_{gg} = 0.1$ ,  $s_{12} = s_{1g} = s_{2g} = 10^{-5}$ ,  $s_{1s} = 0.2$ ,  $s_{2s} = 0.15$ , and  $s_{3s} = 10^{-5}$ . Scenario 2:  $s_{11} = s_{22} = s_{gg} = 0.1$ ,  $s_{12} = s_{1g} = s_{2g} = 10^{-5}$ ,  $s_{1s} = 0.2$ ,  $s_{2s} = 0.3$ , and  $s_{3s} = 10^{-5}$ . Scenario 3:  $s_{11} = s_{22} = 0.2$ ,  $s_{gg} = 0.1$ ,  $s_{12} = 0.15$ ,  $s_{1g} = 10^{-5}$ ,  $s_{2g} = 0.075$ ,  $s_{1s} = 0.2$ ,  $s_{2s} = 0.3$ , and  $s_{3s} = 10^{-5}$ . (For interpretation of the references to color in this figure, the reader is referred to the web version of this article.)

We demonstrated that away from the interface,  $\mathbf{F}_{ij}^{int}$  generates an additional “virial” pressure and derived an analytical expression for this pressure, which can be used to compute the total pressure in PF-SPH simulations. We further demonstrated the PF-SPH model’s accuracy by simulating flow of a droplet between two parallel plates and spreading of a droplet on a horizontal surface and comparing the results of the simulations with the analytical solutions.

In numerical models of multiscale systems, it is difficult, if not impossible, to sufficiently resolve all length scales. For example, in a typical porous medium, the size of a pore is much smaller than the size of the porous domain. Pore throats are much smaller than the pore size, and fluid bubbles could be much smaller than the average size of the pore throats. Consequently, in a numerical model of the multiphase flow in porous media, it is prohibitively expensive to achieve an adequate resolution of small fluid bubbles and other features, such as films of a wetting fluid surrounding solid phase. One attractive feature of the PF-SPH method is that the forces  $\mathbf{F}_{ij}^{int}$  generate surface tension and contact angles in the same way as molecular forces. Because of this, the PF-SPH model remains numerically stable even when some features of the simulated system (e.g., small bubbles) are not adequately resolved. This is in contrast to other numerical models, which directly implement the Young–Laplace boundary condition. The direct implementation of the Young–Laplace boundary condition requires calculations of the normal vectors to, and curvature of, the interface. The calculation of curvatures and normals can become very noisy if the interface between two fluids is not adequately resolved, which can, in turn, lead to numerical instabilities. We should note that, unlike molecular forces, the  $\mathbf{F}_{ij}^{int}$  forces are “soft,” i.e., the magnitude of  $\mathbf{F}_{ij}^{int}$  is finite for the zero-distance between the particles. Because of this, the  $\mathbf{F}_{ij}^{int}$  forces do not impose time step constraints in addition to the time constraints (23) in the standard SPH method [20].

We demonstrated that the PF-SPH model is capable of simulating complex multiphase flows, such as a three-phase flow in a porous medium. We simulated flows of two liquids and a gas in a two-dimensional porous medium, made of solid obstacles of irregular shape. Liquids were assumed to be 1000 times denser and 100 times more viscous than the gas phase, the ratios typical for water/oil/gas systems. We studied the effect of wettability and surface tensions between different phases on the fluid flow and residual saturation of the fluid phases. Most of the grid-based multiphase flow models are limited to no more than two fluid phases. To the best of our knowledge, the PF-SPH model is one of very few models that can reliably deal with three-phase pore-scale flows.

## Acknowledgements

The authors wish to thank Prof. J.J. Monaghan for bringing the work of Rayleigh on a molecular theory of capillarity to their attention. The authors gratefully acknowledge funding support from the Applied Mathematics Program within the U.S. Department of Energy's (DOE) Office of Advanced Scientific Computing Research (ASCR) as part of the Early Career Award, “New Dimension Reduction Methods and Scalable Algorithms for Multiscale Nonlinear Phenomena” (60105). Pacific Northwest National Laboratory is operated by Battelle for the DOE under Contract DE-AC05-76RL01830.

## Appendix A. Integral expression for surface tension

For compactness, in this section, we provide derivations only in two spacial dimensions. Derivations in three spacial dimensions are similar, and the final results are identical to the result of Maxwell [18], obtained for a fluid made of particles (molecules) that do not move at the static equilibrium and interact with each other via pairwise forces.

For simplicity, we assume the fluids are separated by a flat interface. Without loss of generality, we set the interface at  $y = 0$  and assume that the subspace  $\mathcal{I}_1 = (x, y < 0)$  is occupied by Phase 1, while Phase 2 occupies the subspace  $\mathcal{I}_2 = (x, y > 0)$ . According to Eq. (28), the surface tension  $\sigma$  is given as:

$$\sigma = \int_{y_1}^{y_2} [T_{xx}(y) - T_{yy}(y)] dy, \quad (\text{A.1})$$

where  $y_1 = -y'$ ,  $y_2 = y'$ , and  $y' \gg \eta$ .

Under static condition, the convection component of the stress is equal to zero, and the stress is given by Eq. (26). For the geometry considered here,  $T_{xx}$  can be written as:

$$\begin{aligned} T_{xx}(\mathbf{x}) = & -\frac{1}{2} \sum_{i \in \mathcal{I}_1} \sum_{j \in \mathcal{I}_1} \phi_{11}(r_{ij}) \frac{(\mathbf{r}_{ij(x)})^2}{r_{ij}} \int_0^1 \tilde{\psi}_\eta(\mathbf{x} - (s\mathbf{r}_i + (1-s)\mathbf{r}_j)) ds \\ & -\frac{1}{2} \sum_{i \in \mathcal{I}_2} \sum_{j \in \mathcal{I}_2} \phi_{22}(r_{ij}) \frac{(\mathbf{r}_{ij(x)})^2}{r_{ij}} \int_0^1 \tilde{\psi}_\eta(\mathbf{x} - (s\mathbf{r}_i + (1-s)\mathbf{r}_j)) ds \\ & -\frac{1}{2} \sum_{i \in \mathcal{I}_1} \sum_{j \in \mathcal{I}_2} \phi_{12}(r_{ij}) \frac{(\mathbf{r}_{ij(x)})^2}{r_{ij}} \int_0^1 \tilde{\psi}_\eta(\mathbf{x} - (s\mathbf{r}_i + (1-s)\mathbf{r}_j)) ds \\ & -\frac{1}{2} \sum_{i \in \mathcal{I}_2} \sum_{j \in \mathcal{I}_1} \phi_{21}(r_{ij}) \frac{(\mathbf{r}_{ij(x)})^2}{r_{ij}} \int_0^1 \tilde{\psi}_\eta(\mathbf{x} - (s\mathbf{r}_i + (1-s)\mathbf{r}_j)) ds, \end{aligned} \quad (\text{A.2})$$

where  $\mathbf{r}_{ij(x)}$  is the  $x$  component of the vector  $\mathbf{r}_{ij}$ .

Noting that  $\phi_{12}(r_{ij})\frac{(\mathbf{r}_{ij(x)})^2}{r_{ij}} = \phi_{21}(r_{ji})\frac{(\mathbf{r}_{ji(x)})^2}{r_{ji}}$ , we rewrite the above expression as:

$$T_{xx}(\mathbf{x}) = -\frac{1}{2} \sum_{i \in \mathcal{I}_1} \sum_{j \in \mathcal{I}_1} \phi_{11}(r_{ij}) \frac{(\mathbf{r}_{ij(x)})^2}{r_{ij}} \int_0^1 \tilde{\psi}_\eta(\mathbf{x} - (s\mathbf{r}_i + (1-s)\mathbf{r}_j)) ds \quad (\text{A.3})$$

$$\begin{aligned} & -\frac{1}{2} \sum_{i \in \mathcal{I}_2} \sum_{j \in \mathcal{I}_2} \phi_{22}(r_{ij}) \frac{(\mathbf{r}_{ij(x)})^2}{r_{ij}} \int_0^1 \tilde{\psi}_\eta(\mathbf{x} - (s\mathbf{r}_i + (1-s)\mathbf{r}_j)) ds \\ & - \sum_{i \in \mathcal{I}_1} \sum_{j \in \mathcal{I}_2} \phi_{12}(r_{ij}) \frac{(\mathbf{r}_{ij(x)})^2}{r_{ij}} \int_0^1 \tilde{\psi}_\eta(\mathbf{x} - (s\mathbf{r}_i + (1-s)\mathbf{r}_j)) ds. \end{aligned} \quad (\text{A.4})$$

To evaluate the integral of  $T_{xx}$ , we approximate the sums in the definition of the stress tensor by integrals:

$$T_{xx} = T_{xx}^{(11)} + T_{xx}^{(22)} + T_{xx}^{(12)}, \quad (\text{A.5})$$

where

$$T_{xx}^{(11)}(\mathbf{x}) \approx -\frac{1}{2} n_1^2 \int_{\mathcal{I}_1} \int_{\mathcal{I}_1} \phi_{11}(r_{ij}) \frac{(\mathbf{r}_{ij(x)})^2}{r_{ij}} \int_0^1 \tilde{\psi}_\eta(\mathbf{x} - (s\mathbf{r}' + (1-s)\mathbf{r}'')) ds d\mathbf{r}' d\mathbf{r}'', \quad (\text{A.6})$$

$$T_{xx}^{(22)}(\mathbf{x}) \approx -\frac{1}{2} n_2^2 \int_{\mathcal{I}_2} \int_{\mathcal{I}_2} \phi_{22}(r_{ij}) \frac{(\mathbf{r}_{ij(x)})^2}{r_{ij}} \int_0^1 \tilde{\psi}_\eta(\mathbf{x} - (s\mathbf{r}' + (1-s)\mathbf{r}'')) ds d\mathbf{r}' d\mathbf{r}'', \quad (\text{A.7})$$

and

$$T_{xx}^{(12)}(\mathbf{x}) \approx -n_1 n_2 \int_{\mathcal{I}_1} \int_{\mathcal{I}_2} \phi_{12}(r_{ij}) \frac{(\mathbf{r}_{ij(x)})^2}{r_{ij}} \int_0^1 \tilde{\psi}_\eta(\mathbf{x} - (s\mathbf{r}' + (1-s)\mathbf{r}'')) d\mathbf{r}' d\mathbf{r}''. \quad (\text{A.8})$$

Next, we introduce the notation:

$$\begin{aligned} \mathbf{r}' &= (x', y'), \quad \mathbf{r}'' = (x'', y''), \\ \boldsymbol{\rho} &= \mathbf{r}' - \mathbf{r}'' = (\rho_1, \rho_2), \\ \mathbf{R} &= \frac{1}{2}(\mathbf{r}' + \mathbf{r}'') = (R_1, R_2), \end{aligned} \quad (\text{A.9})$$

and rewrite  $T_{xx}^{(11)}$ ,  $T_{xx}^{(22)}$ , and  $T_{xx}^{(12)}$  as:

$$\begin{aligned} T_{xx}^{(11)} &= -\frac{1}{2} n_1^2 \int_{-\infty}^{\infty} dx' \int_{-\infty}^0 dy' \int_{-\infty}^{\infty} dx'' \int_{-\infty}^0 dy'' \phi_{11}(|\mathbf{r}' - \mathbf{r}''|) \frac{(x' - x'')^2}{|\mathbf{r}' - \mathbf{r}''|} \\ &\times \int_0^1 \tilde{\psi}_\eta(\mathbf{x} - (s\mathbf{r}' + (1-s)\mathbf{r}'')) ds, \end{aligned} \quad (\text{A.10})$$

$$\begin{aligned} T_{xx}^{(22)} &= -\frac{1}{2} n_2^2 \int_{-\infty}^{\infty} dx' \int_{-\infty}^0 dy' \int_{-\infty}^{\infty} dx'' \int_{-\infty}^0 dy'' \phi_{22}(|\mathbf{r}' - \mathbf{r}''|) \frac{(x' - x'')^2}{|\mathbf{r}' - \mathbf{r}''|} \\ &\times \int_0^1 \tilde{\psi}_\eta(\mathbf{x} - (s\mathbf{r}' + (1-s)\mathbf{r}'')) ds, \end{aligned} \quad (\text{A.11})$$

and

$$T_{xx}^{(12)} = -\frac{1}{2} n_1^2 \int_{-\infty}^{\infty} dx' \int_{-\infty}^0 dy' \int_{-\infty}^{\infty} dx'' \int_{-\infty}^0 dy'' \phi_{12}(|\mathbf{r}' - \mathbf{r}''|) \frac{(x' - x'')^2}{|\mathbf{r}' - \mathbf{r}''|}$$

$$\times \int_0^1 \tilde{\psi}_\eta(\mathbf{x} - (s\mathbf{r}' + (1-s)\mathbf{r}'')) ds. \quad (\text{A.12})$$

Similarly,  $T_{yy} = T_{yy}^{(11)} + T_{yy}^{(22)} + T_{yy}^{(12)}$ , where

$$T_{yy}^{(11)} = -\frac{1}{2}n_1^2 \int_{-\infty}^{\infty} dx' \int_{-\infty}^0 dy' \int_{-\infty}^{\infty} dx'' \int_{-\infty}^0 dy'' \phi_{11}(|\mathbf{r}' - \mathbf{r}''|) \frac{(y' - y'')^2}{|\mathbf{r}' - \mathbf{r}''|}$$

$$\times \int_0^1 \tilde{\psi}_\eta(\mathbf{x} - (s\mathbf{r}' + (1-s)\mathbf{r}'')) ds, \quad (\text{A.13})$$

$$T_{yy}^{(22)} = -\frac{1}{2}n_1^2 \int_{-\infty}^{\infty} dx' \int_{-\infty}^0 dy' \int_{-\infty}^{\infty} dx'' \int_{-\infty}^0 dy'' \phi_{22}(|\mathbf{r}' - \mathbf{r}''|) \frac{(y' - y'')^2}{|\mathbf{r}' - \mathbf{r}''|}$$

$$\times \int_0^1 \tilde{\psi}_\eta(\mathbf{x} - (s\mathbf{r}' + (1-s)\mathbf{r}'')) ds, \quad (\text{A.14})$$

and

$$T_{yy}^{(12)} = -\frac{1}{2}n_1^2 \int_{-\infty}^{\infty} dx' \int_{-\infty}^0 dy' \int_{-\infty}^{\infty} dx'' \int_{-\infty}^0 dy'' \phi_{12}(|\mathbf{r}' - \mathbf{r}''|) \frac{(y' - y'')^2}{|\mathbf{r}' - \mathbf{r}''|}$$

$$\times \int_0^1 \tilde{\psi}_\eta(\mathbf{x} - (s\mathbf{r}' + (1-s)\mathbf{r}'')) ds. \quad (\text{A.15})$$

Splitting the stress components into contributions from different types of forces, we obtain:

$$\sigma = \int_{y_1}^{y_2} \left( (T_{11}^{11}(y) - T_{22}^{11}(y)) + (T_{11}^{22}(y) - T_{22}^{22}(y)) + (T_{11}^{12}(y) - T_{22}^{12}(y)) \right) dy. \quad (\text{A.16})$$

Next, choose

$$\tilde{\psi}_\eta(\mathbf{x}) = \psi_\eta(x)\psi_\eta(y), \quad (\text{A.17})$$

where  $\psi_\eta$  is chosen so that

$$\psi_\eta(x) = \frac{1}{\eta}\psi\left(\frac{x}{\eta}\right), \quad \psi(x) = \begin{cases} 1 & \text{if } x \in (-1/2, 1/2), \\ 0 & \text{otherwise,} \end{cases} \quad (\text{A.18})$$

and

$$\Psi_\eta(y_1, y_2, R_2) = \int_{y_1}^{y_2} \psi_\eta(y - R_2) dy = \begin{cases} 0 & \text{if } R_2 < y_1 - \frac{1}{2}\eta, \\ \frac{1}{\eta}(-y_1 + R_2 + \frac{1}{2}\eta) & \text{if } y_1 - \frac{1}{2}\eta \leq R_2 < y_1 + \frac{1}{2}\eta, \\ 1 & \text{if } y_1 + \frac{1}{2}\eta \leq R_2 < z_2 - \frac{1}{2}\eta, \\ \frac{1}{\eta}(y_2 - R_2 + \frac{1}{2}\eta) & \text{if } y_2 - \frac{1}{2}\eta \leq R_2 < y_2 + \frac{1}{2}\eta, \\ 0 & \text{if } R_2 \geq y_2 + \frac{1}{2}\eta. \end{cases} \quad (\text{A.19})$$

Thus,

$$\tilde{\psi}_\eta(\mathbf{x} - (s\mathbf{r}' + (1-s)\mathbf{r}'')) = \psi_\eta(x - (sx' + (1-s)x''))\psi_\eta(y - (sy' + (1-s)y'')), \quad (\text{A.20})$$

and we approximate

$$\begin{aligned}
& \int_0^1 \tilde{\psi}_\eta(\mathbf{x} - (s\mathbf{r}' - (1-s)\mathbf{r}'')) ds \\
& \approx \int_0^1 \psi_\eta(x - (\frac{1}{2}x' + (1-\frac{1}{2})x'')) \psi_\eta(y - (\frac{1}{2}y' + (1-\frac{1}{2})y'')) ds \\
& = \psi_\eta(x - R_1) \psi_\eta(y - R_2).
\end{aligned} \tag{A.21}$$

Inserting this into Eqs. (A.10) and (A.13) and changing variables of integration from  $\mathbf{r}', \mathbf{r}''$  to  $\boldsymbol{\rho}, \mathbf{R}$ , we obtain:

$$\begin{aligned}
& T_{xx}^{(11)} - T_{yy}^{(11)} \\
& \approx -\frac{1}{2} n_1^2 \int_{-\infty}^{\infty} dR_1 \int_{-\infty}^0 dR_2 \int_{S(\mathbf{R})} d\boldsymbol{\rho} \phi_{11}(|\boldsymbol{\rho}|) \frac{\rho_1^2 - \rho_2^2}{|\boldsymbol{\rho}|} \psi_\eta(x - R_1) \psi_\eta(y - R_2).
\end{aligned} \tag{A.22}$$

The region  $S(\mathbf{R})$  of integration with respect to  $\boldsymbol{\rho}$  is defined by

$$\rho_1 \in (-\infty, \infty), \quad 2R_2 < \rho_2 < -2R_2.$$

This follows from  $y' = R_2 + \frac{1}{2}\rho_2 < 0$ , and  $y'' = R_2 - \frac{1}{2}\rho_2 < 0$ . Because  $S(\mathbf{R})$  is independent of  $R_1$ , integration with respect to  $R_1$  can be carried out first. Because of the normalization condition built into the choice of  $\psi_\eta$ ,

$$\int_{-\infty}^{\infty} \psi_\eta(x - R_1) dR_1 = 1.$$

Thus,

$$T_{xx}^{(11)} - T_{yy}^{(11)} \approx -\frac{1}{2} n_1^2 \int_{-\infty}^0 dR_2 \int_{S(\mathbf{R})} d\boldsymbol{\rho} \phi_{11}(|\boldsymbol{\rho}|) \frac{\rho_1^2 - \rho_2^2}{|\boldsymbol{\rho}|} \psi_\eta(y - R_2).$$

Next, observe that, because of symmetry of  $S(\mathbf{R})$  and because the function under the integral depends only on  $\rho_1^2$  and  $\rho_2^2$ ,

$$\int_{S(\mathbf{R})} \phi_{11}(|\boldsymbol{\rho}|) \frac{\rho_1^2 - \rho_2^2}{|\boldsymbol{\rho}|} d\boldsymbol{\rho} = 4 \int_{\hat{S}(\mathbf{R})} \phi_{11}(|\boldsymbol{\rho}|) \frac{\rho_1^2 - \rho_2^2}{|\boldsymbol{\rho}|} d\boldsymbol{\rho},$$

where

$$\hat{S}(\mathbf{R}) = \{\boldsymbol{\rho} : \rho_1 > 0, 0 < \rho_2 < -2R_2\}.$$

Now, we change the variable of integration in the  $\boldsymbol{\rho}$ -integral to polar coordinates  $t, \xi$ . Then,

$$T_{xx}^{(11)} - T_{yy}^{(11)} \approx -2n_1^2 \int_{-\infty}^0 dR_2 \int_{D^{(11)}(R_2, t)} dt d\xi \phi_{11}(t) t^2 \cos^2 2\xi \psi_\eta(y - R_2), \tag{A.23}$$

where the region of integration  $D^{(11)}(R_2, t)$  with respect to  $t, \xi$  is described as follows: if  $t \in (0, -2R_2)$ , then  $\xi \in (0, \pi/2)$ . If  $t \geq -2R_2$ , then  $\xi \in (0, \hat{\xi})$  with

$$\hat{\xi} = \sin^{-1} \left( -\frac{2R_2}{t} \right).$$

To simplify the notation, write:

$$g(u) = \sin^{-1} u, \tag{A.24}$$

so that

$$\hat{\xi} = g \left( -\frac{2R_2}{t} \right) = -g \left( \frac{2R_2}{t} \right). \tag{A.25}$$

Similarly,

$$T_{xx}^{(22)} - T_{yy}^{(22)} \approx -2n_1^2 \int_{-\infty}^0 dR_2 \int_{D^{(22)}(R_2,t)} dt d\xi \phi_{22}(t) t^2 \cos^2 2\xi \psi_\eta(y - R_2), \quad (\text{A.26})$$

where the region of integration  $D^{(22)}(R_2, t)$  with respect to  $t, \xi$  is described as follows: if  $t \in (0, 2R_2)$ , then  $\xi \in (0, \pi/2)$ . If  $t \geq 2R_2$ , then  $\xi \in (0, \hat{\xi})$  and

$$\hat{\xi} = \sin^{-1} \left( \frac{2R_2}{t} \right). \quad (\text{A.27})$$

The contribution from the interaction forces between particles of different phases has the form:

$$\begin{aligned} T_{xx}^{(12)}(y) - T_{yy}^{(12)}(y) &= -n_2 n_2 \int_{-\infty}^0 dR_2 \psi_\eta(y - R_2) \int_{D^{(12,1)}(R_2,t)} dt d\xi \phi_{12}(t) t^2 \cos 2\xi \\ &\quad - n_1 n_2 \int_0^\infty dR_2 \psi_\eta(y - R_2) \int_{D^{(12,2)}(R_2,t)} dt d\xi \phi_{12}(t) t^2 \cos 2\xi. \end{aligned} \quad (\text{A.28})$$

The last two integrals are equal, so we only need to calculate the first one. Thus,

$$T_{xx}^{(12)}(y) - T_{yy}^{(12)}(y) = -2n_2 n_2 \int_{-\infty}^0 dR_2 \psi_\eta(y - R_2) \int_{D^{(12,1)}(R_2,t)} dt d\xi \phi_{12}(t) t^2 \cos 2\xi, \quad (\text{A.29})$$

where  $D^{(12,1)}(R_2, t)$  is described as follows:

$$D^{(12,1)}(R_2, t) = \{(t, \xi) : -2R_2 < t < \infty, \pi + \hat{\xi} < \xi < 2\pi - \hat{\xi}\}, \quad (\text{A.30})$$

where

$$\hat{\xi} = \sin^{-1} \left( -\frac{2R_2}{t} \right). \quad (\text{A.31})$$

To calculate the contributions from particles of the same phase, we first compute:

$$T_{xx}^{(11)}(y) - T_{yy}^{(11)}(y) = -n_1^2 \int_{-\infty}^0 dR_2 \psi_\eta(y - R_2) \int_{-2R_2}^\infty dt \phi_{11}(t) t^2 \sin 2\hat{\xi}.$$

Integrating in  $y$ , we obtain:

$$\int_{y_1}^{y_2} T_{xx}^{(11)}(y) - T_{yy}^{(11)}(y) dy = -\frac{1}{3} n_1^2 \int_0^\infty \phi_{11}(t) t^3 dt. \quad (\text{A.32})$$

Similarly,

$$\int_{y_1}^{y_2} T_{xx}^{(22)}(y) - T_{yy}^{(22)}(y) dy = -\frac{1}{3} n_2^2 \int_0^\infty \phi_{22}(t) t^3 dt. \quad (\text{A.33})$$

To compute the contribution from particles of different phases to the surface tension, we note that

$$T_{xx}^{(12)}(y) - T_{yy}^{(12)}(y) = 2n_1 n_2 \int_{-\infty}^0 dR_2 \psi_\eta(y - R_2) \int_{2R_2}^\infty dt \phi_{12}(t) t^2 \sin 2\hat{\xi}. \quad (\text{A.34})$$

Integrating in  $y$ , we obtain:

$$\int_{y_1}^{y_2} T_{xx}^{(12)}(y) - T_{yy}^{(12)}(y) dy = \frac{2}{3} n_1 n_2 \int_0^\infty \phi_{12}(t) t^3 dt. \quad (\text{A.35})$$

Combining equations (A.16), (A.32), (A.33), and (A.35), we find:

$$\sigma = -\frac{1}{3} n_1^2 \int_0^\infty \phi_{11}(t) t^3 dt - \frac{1}{3} n_2^2 \int_0^\infty \phi_{22}(t) t^3 dt + \frac{2}{3} n_1 n_2 \int_0^\infty \phi_{12}(t) t^3 dt. \quad (\text{A.36})$$

## Appendix B. Integral expression for pressure

Pressure in the  $i$ -th fluid phase ( $i = 1, 2$ ) far away from the interface separating Fluids 1 and 2 is given by

$$p_i = -T_{xx}^{ii} = -T_{yy}^{ii}. \quad (\text{B.1})$$

For  $i = 1$ ,  $T_{xx}^{11}$  can be found from Eq. (A.23) as:

$$T_{xx}^{(11)} \approx -4 \frac{1}{2} n_1^2 \int_{-\infty}^0 dR_2 \int_{D^{(11)}(R_2, t)} dt d\xi \phi_{11}(t) t^2 \cos^2 \xi \psi_\eta(y - R_2), \quad (\text{B.2})$$

where the region of integration  $D^{(11)}(R_2, t)$  is defined in Appendix A.

We choose a negative  $y$  with large  $|y|$  so the support of  $\psi_\eta(y - R_2)$  is located inside the interval  $(-\infty, 0)$ . Because the range of the force  $\phi_{11}(t)$  is finite,  $y$  can be moved further away from the interface, if necessary, to ensure that  $\phi_{11}(t) = 0$  for all  $t > -2R_2$ . In that case, the region of integration  $D^{(11)}(R_2, t)$  is simply  $\xi \in (0, 2\pi)$ ,  $t < -2R_2$ , and the integration in  $t$  can be extended to  $(0, \infty)$  without changing the value of the integral. This yields:

$$p_1 = \frac{1}{2} n_1^2 \int_{-\infty}^0 dR_2 \int_0^\infty \int_0^{2\pi} dt d\xi \phi_{11}(t) t^2 \cos^2 \xi \psi_\eta(y - R_2). \quad (\text{B.3})$$

Because support of  $\psi_\eta(y - R_2)$  rests inside the interval of integration in  $R_2$ , this integral is equal to one. The integral with respect to  $\phi$  can be easily computed directly. The result is:

$$p_1 = \frac{1}{2} \pi n_1^2 \int_0^\infty \phi_{11}(t) t^2 dt. \quad (\text{B.4})$$

## References

- [1] S. Adami, X. Hu, N. Adams, A new surface-tension formulation for multi-phase SPH using a reproducing divergence approximation, *J. Comput. Phys.* 229 (13) (2010) 5011–5021.
- [2] M.P. Allen, D.J. Tildesley, *Computer Simulation of Liquids*, Oxford University Press, 1989.
- [3] U. Bandara, A. Tartakovsky, M. Oostrom, B. Palmer, J. Grate, C. Zhang, Smoothed particle hydrodynamics pore-scale simulations of unstable immiscible flow in porous media, *Adv. Water Resour.* 62 (Part C) (2013) 356–369.
- [4] D. Bonn, J. Eggers, J. Indekeu, J. Meunier, E. Rolley, Wetting and spreading, *Rev. Mod. Phys.* 81 (May 2009) 739–805.
- [5] J. Brackbill, D.B. Kothe, C. Zemach, A continuum method for modeling surface tension, *J. Comput. Phys.* 100 (2) (1992) 335–354.
- [6] R. Cox, The dynamics of the spreading of liquids on a solid surface. Part I. Viscous flow, *J. Fluid Mech.* 168 (1986) 169–194.
- [7] P. de Gennes, Wetting: statics and dynamics, *Rev. Mod. Phys.* 57 (3) (1985) 827–863.
- [8] M.I. Dragila, N. Weisbrod, Fluid motion through an unsaturated fracture junction, *Water Resour. Res.* 40 (2) (2004).
- [9] E. Dussan V, On the spreading of liquids on solid surfaces: static and dynamic contact lines, *Annu. Rev. Fluid Dyn.* 11 (1979) 371–400.
- [10] S.O.R. Fedkiw, *Level Set Methods and Dynamic Implicit Surfaces*, Springer, 2003.
- [11] R.J. Hardy, Formulas for determining local properties in molecular-dynamics simulations: shock waves, *J. Chem. Phys.* 76 (1) (1982) 622–628.
- [12] D.W. Holmes, J.R. Williams, P. Tilke, Smooth particle hydrodynamics simulations of low Reynolds number flows through porous media, *Int. J. Numer. Anal. Methods Geomech.* 35 (4) (2011) 419–437.
- [13] X. Hu, N. Adams, A multi-phase SPH method for macroscopic and mesoscopic flows, *J. Comput. Phys.* 213 (2) (2006) 844–861.
- [14] H. Huang, P. Meakin, Three-dimensional simulation of liquid drop dynamics within unsaturated vertical Hele-Shaw cells, *Water Resour. Res.* 44 (3) (2008).
- [15] C. Huh, L. Scriven, Hydrodynamic model of steady movement of a solid/liquid/fluid contact line, *J. Colloid Interface Sci.* 35 (1) (1971) 85–101.
- [16] J. Kordilla, A. Tartakovsky, T. Geyer, A smoothed particle hydrodynamics model for droplet and film flow on smooth and rough fracture surfaces, *Adv. Water Resour.* 59 (0) (2013) 1–14.
- [17] M. Liu, P. Meakin, H. Huang, Dissipative particle dynamics simulation of fluid motion through an unsaturated fracture and fracture junction, *J. Comput. Phys.* 222 (1) (2007) 110–130.
- [18] J. Maxwell, *The Scientific Papers of J.M. Maxwell, Capillary Actions*, vol. 2, Cambridge University Press, 1890, 541 pp.
- [19] P. Meakin, A.M. Tartakovsky, Modeling and simulation of pore scale multiphase fluid flow and reactive transport in fractured and porous media, *Rev. Geophys.* 47 (2009) RG3002.

- [20] J.J. Monaghan, Smoothed particle hydrodynamics, *Rep. Prog. Phys.* 68 (8) (2005) 1703.
- [21] J. Morris, Simulating surface tension with smoothed particle hydrodynamics, *Int. J. Numer. Methods Fluids* 33 (3) (2000) 333–353.
- [22] J.P. Morris, P.J. Fox, Y. Zhu, Modeling low Reynolds number incompressible flows using SPH, *J. Comput. Phys.* 136 (1) (1997) 214–226.
- [23] N.J. Quinlan, M. Basa, M. Lastiwka, Truncation error in mesh-free particle methods, *Int. J. Numer. Methods Eng.* 66 (13) (2006) 2064–2085.
- [24] A.Q. Raeini, M.J. Blunt, B. Bijeljic, Modelling two-phase flow in porous media at the pore scale using the volume-of-fluid method, *J. Comput. Phys.* 231 (17) (2012) 5653–5668.
- [25] J.J.S. Rowlinson, B. Widom, *Molecular Theory of Capillarity*, vol. 8, Courier Dover Publications, 2002.
- [26] P. Sheng, M. Zhou, Immiscible-fluid displacement: contact-line dynamics and the velocity-dependent capillary pressure, *Phys. Rev. A* 45 (8) (1992) 5694.
- [27] L.H. Tanner, The spreading of silicone oil drops on horizontal surfaces, *J. Phys. D, Appl. Phys.* 12 (9) (1979) 1473 (Email alert RSS feed).
- [28] A. Tartakovsky, P. Meakin, Modeling of surface tension and contact angles with smoothed particle hydrodynamics, *Phys. Rev. E* 72 (2) (2005) 026301.
- [29] A. Tartakovsky, P. Meakin, A. Ward, Smoothed particle hydrodynamics model of non-aqueous phase liquid flow and dissolution, *Transp. Porous Media* 76 (2009) 11–34.
- [30] A.M. Tartakovsky, K.F. Ferris, P. Meakin, Lagrangian particle model for multiphase flows, *Comput. Phys. Commun.* 180 (10) (2009) 1874–1881.
- [31] A.M. Tartakovsky, P. Meakin, Simulation of free-surface flow and injection of fluids into fracture apertures using smoothed particle hydrodynamics, *Vadose Zone J.* 4 (3) (2005) 848–855.
- [32] A.M. Tartakovsky, P. Meakin, Pore scale modeling of immiscible and miscible fluid flows using smoothed particle hydrodynamics, *Adv. Water Resour.* 29 (10) (2006) 1464–1478.
- [33] A.M. Tartakovsky, A.L. Ward, P. Meakin, Pore-scale simulations of drainage of heterogeneous and anisotropic porous media, *Phys. Fluids* 19 (10) (2007) 103301.
- [34] P. Tomin, I. Lunati, Hybrid multiscale finite volume method for two-phase flow in porous media, *J. Comput. Phys.* 250 (2013) 293–307.